

Simulating the evolution of soot mixing state with a particle-resolved aerosol model

N. Riemer,¹ M. West,² R. A. Zaveri,³ and R. C. Easter³

Abstract. The mixing state of soot particles in the atmosphere is of crucial importance for assessing their climatic impact, since it governs their chemical reactivity, cloud condensation nuclei activity and radiative properties. To improve the mixing state representation in models, we present a new approach, the stochastic particle-resolved model PartMC-MOSAIC, which explicitly resolves the composition of individual particles in a given population of different types of aerosol particles. This approach accurately tracks the evolution of the mixing state of particles due to emission, dilution, condensation and coagulation. To make this direct stochastic particle-based method practical, we implemented a new multiscale stochastic coagulation method. With this method we achieved optimal efficiency for applications when the coagulation kernel is highly non-uniform, as is the case for many realistic applications. PartMC-MOSAIC was applied to an idealized urban plume case representative of a large urban area to simulate the evolution of carbonaceous aerosols of different types due to coagulation and condensation. For this urban plume scenario we quantified the individual processes that contribute to the aging of the aerosol distribution, illustrating the capabilities of our modeling approach. The results showed for the first time the multidimensional structure of particle composition, which is usually lost in internally-mixed sectional or modal aerosol models.

1. Introduction

Soot particles are an important constituent of the atmospheric aerosol, since they participate in tropospheric chemistry [Saathoff *et al.*, 2001] and affect human pulmonary health [Pope and Dockery, 1996]. Because of its ability to absorb light [Horvath and Trier, 1993], soot is also recognized as an important player in the aerosol radiative forcing of climate at global, regional, and local scales [Menon *et al.*, 2002; Chung and Seinfeld, 2005; Roeckner *et al.*, 2006]. The source of soot particles is the incomplete combustion of carbon containing material, which means that except for natural biomass burning all sources of soot are of anthropogenic origin [Penner, 1995]. The dominant removal process is wet deposition [Ducret and Cachier, 1992]. Soot particles can be transported over long distances reaching remote regions such as the Arctic [Clarke and Noone, 1985; Hansen and Nazarenko, 2004].

The initial composition of soot particles consists of black carbon and organic carbon. The precise mixture depends heavily on the source [Medalia and Rivin, 1982; Andreae and Gelencsér, 2006]. While freshly emitted soot particles are rather hydrophobic and present in an external mixture, their hygroscopic qualities can change due to coagulation with soluble aerosols, condensation of secondary organic and inorganic species, and photochemical processes [Weingartner *et al.*, 1997]. These processes are usually referred to as “aging,” and they determine the particle growth in response to ambient relative humidity and the ability to be activated as cloud condensation nuclei. The aging processes also have a profound effect on the aerosol optical properties.

For example, internally mixed soot shows greater absorptivity compared to externally mixed soot. This effect on radiative properties has been studied by a number of investigators, e.g. Chýlek *et al.* [1995]; Jacobson [2001]; Riemer *et al.* [2003]; Schnaiter *et al.* [2005]; Bond *et al.* [2006]. Measurements show that atmospheric soot particles are internally mixed with other aerosol species in varying proportions, and that the hydrophobic portion of the aerosols decreases significantly as the distance from the sources increases [Andreae *et al.*, 1986; Levin *et al.*, 1996; Okada and Hitzenberger, 2001; Johnson *et al.*, 2005; Cubison *et al.*, 2008].

Since it is well recognized that soot particles contribute to both the direct and indirect/semi-direct climate effect [Lesins *et al.*, 2002; Jacobson, 2000, 2002b; Nenes *et al.*, 2002], an adequate representation of soot and its mixing state is sought for use in both global and regional models, and the parameterization of soot aging is key to determining its atmospheric abundance. Many global models have simulated both (fresh) hydrophobic soot and (aged) hydrophilic soot, which can be considered as a minimal representation of the soot mixing state. Several of the models have assumed that the conversion from hydrophobic to hydrophilic soot can be treated as an exponential decay process, with a half-life of approximately 24 h [Cooke *et al.*, 1999; Lohmann *et al.*, 1999; Koch, 2001; Chung and Seinfeld, 2002]. This approach is a substantial simplification since the conversion rate depends on many different environmental conditions. This has led to more mechanistic approaches, where processes such as condensation of sulfate on soot particles, chemical oxidation and/or coagulation between different particle classes are explicitly modeled to some extent [Wilson *et al.*, 2001; Stier *et al.*, 2005; Tsigaridis and Kanakidou, 2003]. Koch [2001] and Croft *et al.* [2005] compared different aging parameterizations in global models and concluded that the model results critically depend on the respective formulation.

To better understand the soot aging process it is desirable to have models that are capable of representing the aerosol mixing state. From a computational standpoint, if the aerosol mixing state can be defined in terms of A classes of chemical components (e.g., $A = 8$ with sulfate, nitrate,

¹Department of Atmospheric Science, University of Illinois at Urbana-Champaign, Urbana, Illinois, USA

²Department of Mechanical Science and Engineering, University of Illinois at Urbana-Champaign, Urbana, Illinois, USA

³Atmospheric Science and Global Change Division, Pacific Northwest National Laboratory, Richland, Washington, USA

ammonium, sea salt, hydrophobic organics, soluble organics, black carbon, and mineral dust classes), then the mixing state is an A -dimensional space and the size-resolved particle composition distribution is a multivariate function.

Most existing aerosol models, however, represent the particle population only as a bulk, or as a univariate function of a single variable, typically total mass, diameter, or similar. To do this it is generally assumed that the population is either fully externally mixed, or is internally mixed with all particles in the same size bin or mode having the same mixing state. Within this framework the standard methods are sectional, modal, and moment models. Sectional models (e.g. *Weaver et al.* [1994]; *Jacobson* [1997]; *Adams et al.* [1999]; *Zaveri et al.* [2008]) place a grid on the dependent variable space and store the number distribution or mass distribution (or both) on each grid cell. Modal models (e.g. *Whitby et al.* [1991]; *Whitby and McMurray* [1997]; *Wilson et al.* [2001]; *Stier et al.* [2005]; *Binkowski and Shankar* [1995]) represent the particle distribution as a sum of modes, each having a log-normal (or similar) size distribution described by a small number of parameters (typically number, mass, and width). Moment models (e.g. *McGraw* [1997]) do not explicitly resolve the distribution, but rather track a few low-order moments of it.

It is possible to extend the standard aerosol models to handle multivariate distributions, for example a two dimensional distribution that is a function of two species, or a function of volume and area. Such extensions have been investigated for sectional models [*Fassi-Fihri et al.*, 1997], modal models [*Brock et al.*, 1988], and moment models [*Yoon and McGraw*, 2004a, b]. All such models, however, require storage and computation that scale exponentially in the number of independent variables A . For the model we develop here with $A = 20$ species, fully-resolved multivariate sectional, modal, or moment models are infeasibly expensive. For example, a sectional model normally uses on the order of 8–20 size bins to adequately resolve a univariate aerosol distribution, and even then will suffer from numerical diffusion [*Dhaniyala and Weaver*, 1996; *Wu and Biswas*, 1998]. An A -dimensional distribution would thus require 8^A – 20^A bins, which is infeasible unless A is much smaller than our 20 species. In contrast, the particle-resolved methods developed in this paper scale with the number of particles, not the dimension of the space they are in.

While traditional univariate aerosol models are too expensive if extended to resolve multivariate aerosol mixing states with more than a few dimensions, there have been a number of extensions proposed to resolve the mixing state to some extent. One example of methods that somewhat resolve the mixing state are the so-called source oriented models developed by *Eldering and Cass* [1996] *Kleeman et al.* [1997], and *Kleeman and Cass* [1998] for regional scale modeling. In these models, the particles of different sources remain externally mixed and a number of individual size distributions (usually about ten) are tracked, while their mixing states change due to condensation of secondary substances. However, because the main focus of their studies was the prediction of particle mass size distributions, the changes in number concentrations and particle mixing states due to self- and hetero-coagulation of particles from different sources was ignored. Coagulation between aerosol particles is important if one is interested in predicting the number size distribution, especially under polluted conditions or if long residence times are considered [*Zhang and Wexler*, 2002]. Nevertheless, the source-oriented approach allows the attribution of pollutants to specific sources and is useful for designing emission control strategies [*Kleeman and Cass*, 1998; *Kleeman et al.*, 1999]. It was used in the framework of a Lagrangian trajectory model, compared to measurements by *Bhave et al.* [2002], and has been extended to a 3D Eulerian model [*Kleeman et al.*, 2001; *Ying et al.*,

2004; *Ying and Kleeman*, 2006]. The Lagrangian version described in *Kleeman and Cass* [1998] treated the mixing state to some extent, with fresh emissions introduced as new size distributions at every hour along the trajectory.

Another variant of mixing state modeling was presented by *Jacobson* [2002a], where a total of 18 interacting aerosol size distributions were considered. His approach was not source oriented to the degree of *Kleeman* and coworkers, since anthropogenic emissions from specific sectors were not resolved, but primary mineral dust, sea-salt, organic matter, and black carbon were treated. Three distributions represented black carbon at different degrees of internal mixing. Coagulation between different particle classes was included, and 11 of the 18 particle classes were used to represent the mixed particles that arise due to coagulation interaction of two primary species. Interactions that would result in the formation of a particle with three different constituents resulted in a “mixed” particle and were not tracked further. Despite this considerable complexity the limitation remained that particles for a certain particle class and size were considered to be internally mixed, and the emissions into the primary particle categories were instantly aged.

Riemer et al. [2003] presented an approach for mixing state modeling of soot using a mesoscale modal modeling framework. Five modes described the composition and size distribution of sub-micron particles, consisting of one externally mixed soot mode, two internally mixed soot-free modes (containing inorganic and organic species), and two internally mixed soot-containing modes. The last two modes thus represented aged soot particles, and aging occurred either by coagulation between modes or by condensation of secondary substances. While this treatment allowed the distinction between fresh and “aged” soot, the simplifying assumption was made that each mode itself is internally mixed.

Here we present a particle-resolved model, PartMC, that explicitly stores the composition of many individual aerosol particles (about 10^5) within a well-mixed computational volume. Relative particle positions within this computational volume are not tracked, but rather the coagulation process is simulated stochastically by assuming that coagulation events are Poisson distributed with a Brownian kernel.

Applying such a Monte Carlo approach for simulating the evolution of particle distributions dates back to *Gillespie* [1975], who developed the exact Stochastic Simulation Algorithm (see also *Gillespie* [1976], *Gillespie* [1977] and *Gillespie* [1992]) to treat the stochastic collision-coalescence process in clouds. Variants of *Gillespie*’s algorithm are widely used in different fields, including simulations of gene regulatory networks [*El Samad et al.*, 2005], chemical kinetics [*Gillespie*, 2007], and sintering in flames [*Wells et al.*, 2006].

Since *Gillespie* [1975] particle-resolved methods have been used to study aerosols by many authors. We do not attempt to give a comprehensive literature survey here. *Babovsky* [1999] and *Eibeck and Wagner* [2001] developed the Mass Flow Algorithm with variable computational/physical particle ratios, *Kolodko and Sabelfeld* [2003] gave relevant error estimates, and *Debry et al.* [2003] coupled it to evaporation and condensation. Somewhat similarly, *Laurenzi et al.* [2002] and *Alfonso et al.* [2008] (based on ideas from *Spouge* [1985]) stored the number of particles with identical composition to reduce memory usage and computational expense while using *Gillespie*’s method. *Guias* [1997] studied convergence of stochastic coagulation to the Smolukowski equation. *Efendiev and Zachariah* [2002] investigated enclosures within aerosols using a particle-based method, while *Maisels et al.* [2004] used particle methods with simultaneous nucleation, coagulation, and surface growth.

While not focused on aerosol simulations, much recent work has investigated efficient simulation methods for

reaction-type Markov processes. Gillespie [2001] developed the tau-leaping method for efficient generation of many events with near-constant rates, with extensions by Gillespie and Petzold [2003]; Rathinam *et al.* [2003]; Cao *et al.* [2006] and others, including for multiscale systems with scale separation in Cao *et al.* [2005]. Multiscale variants of Gillespie’s Stochastic Simulation Algorithm have also been developed by E *et al.* [2007]. Gibson and Bruck [2000] developed the Next Reaction Method for efficient exact sampling, which stores and reuses event calculations for efficiency. Anderson [2007] and Anderson [2008] developed efficient simulation algorithms based on the Next Reaction Method and the tau-leaping method.

For the large number of particles in the simulations in this paper, we used an efficient approximate coagulation method, as described in Section 4 below. This used a binned sampling method to efficiently sample from the highly multiscale coagulation kernel in the presence of a very non-uniform particle size distribution, implemented with a multi-event-per-timestep sampling of the coagulation events. Multi-rate versions of Gillespie’s method have been developed previously by Cao *et al.* [2005] and E *et al.* [2007], but relied on scale separation to average slow event rates over fast timescales. The method used here does not accelerate rare events but it does accelerate the generation of events without scale separation, as needed for the smoothly varying coagulation kernels and particle size distributions. The PartMC coagulation method has storage cost proportional to the number of physical particles, computational cost for evaporation/condensation proportional to the number of particles, and computational cost for coagulation proportional to the number of coagulation events.

PartMC was coupled with the new state-of-the-art aerosol chemistry model MOSAIC [Zaveri *et al.*, 2008], which simulates the gas- and particle-phase chemistries, particle-phase thermodynamics, and dynamic gas-particle mass transfer in a deterministic manner. MOSAIC treats all the important aerosol species, including sulfate, nitrate, chloride, carbonate, ammonium, sodium, calcium, primary organic mass (POM), secondary organic mass, black carbon (BC), and inert organic mass. The coupled model system, PartMC-MOSAIC, accurately predicts number, mass, and composition size distributions, and is therefore suited for applications where any or all of these quantities are required.

Simulating all particles explicitly in a population of aerosol completely eliminates any errors associated with numerical diffusion. As a result, the highly accurate treatment of aerosol dynamics and chemistry makes PartMC-MOSAIC suitable for use as a numerical benchmark of mixing state for more approximate models. It can also be applied to different environments going beyond the example of clear-sky photochemistry shown in this paper, including the in-cloud processing of aerosol, and it can be used to accurately estimate quantities that depend on the mixing state, such as cloud condensation nuclei spectra and optical properties, which we will address in a forthcoming paper. The current version of PartMC is available under the GNU General Public License (GPL) at <http://www.mechse.uiuc.edu/research/mwest/partmc/>, while the MOSAIC code is available upon request from R. A. Zaveri.

This manuscript is organized as follows. In Section 2 we write the governing equations for the coupled gas-aerosol box model and discuss the approximations needed by this model of the physical system. The numerical approximation to the governing equations is given in Section 3, where we introduce the particle-resolved aerosol model PartMC and describe how it is coupled to the gas- and aerosol-chemistry code MOSAIC. In Section 4 we give the efficient coagulation algorithm used by PartMC and verify its performance numerically. Finally, Section 5 demonstrates the capabilities of this new model approach by focusing on the evolution

of the mixing state of soot particles in an idealized urban plume scenario. The main contributions of this paper are: 1) an accelerated stochastic coagulation method for multiscale kernels, 2) the coupling of a particle resolved model with a gas- and aerosol-chemistry code, and 3) an initial study of the soot mixing states present in a typical polluted urban environment.

2. Coupled aerosol-gas governing equations

We consider a Lagrangian parcel framework where we simulate the evolution of aerosol particles and trace gases in single parcel (or volume) of air moving along a specified trajectory. In addition to coagulation and aerosol and gas chemistry, the model treats prescribed emissions of aerosols and gases, and mixing of the parcel with “background air”.

The evolution of atmospheric aerosols is extremely complex, involving interactions between fluid-transport and micro-scale properties of the aerosol particles during coagulation and condensation. A fully resolved simulation of fluid-aerosol interaction cannot capture a large enough system to determine macro-scale aerosol distribution properties. Instead of fully resolved models, it is usual to use a box model locally and store the size distribution of aerosol in a certain physical volume without storing the positions of the particles in three dimensions. Particle interactions such as coagulation are then represented stochastically by a kernel K that defines coagulation probability rates for particles depending on their sizes and compositions. This representation assumes that the mixing timescale is significantly faster than the coagulation and condensation timescales. Equivalently, we are assuming that the aerosol processes are almost Markovian and so a memoryless model is a good approximation to the physics. This assumption underlies all sectional and modal models in use today, as well as our particle-resolved model PartMC, and means that we need only consider the aerosol- and gas-species densities.

An aerosol particle contains mass $\mu_a \geq 0$ of species a , for $a = 1, \dots, A$, so that the particle composition is described by the A -dimensional vector $\vec{\mu} \in \mathbb{R}^A$. μ_{all} (m^3) is the total wet mass of the particle, and $\mu_{\text{dry}} = \mu_{\text{all}} - \mu_{\text{H}_2\text{O}}$ (m^3) is the total dry mass. The cumulative aerosol number distribution at time t and constituent masses $\vec{\mu} \in \mathbb{R}^A$ is $N(\vec{\mu}, t)$ (m^{-3}), which is defined to be the number density of aerosol particles that contain less than μ_a mass of species a , for all $a = 1, \dots, A$. The aerosol number distribution at time t and constituent masses $\vec{\mu} \in \mathbb{R}^A$ is $n(\vec{\mu}, t)$ ($\text{m}^{-3} \text{kg}^{-A}$), which is defined by

$$n(\vec{\mu}, t) = \frac{\partial^A N(\vec{\mu}, t)}{\partial \mu_1 \partial \mu_2 \dots \partial \mu_A}. \quad (1)$$

The concentration of trace gas phase species i at time t is given by $g_i(t)$ (mol m^{-3}), for $i = 1, \dots, G$, so the trace gas phase species concentrations are the G -dimensional vector $\vec{g}(t) \in \mathbb{R}^G$. We assume that the aerosol and gas species are numbered so that the first C species of each undergo gas to particle conversion, and that they are in the same order so that gas species i converts to aerosol species i , for $i = 1, \dots, C$.

The environment is described by temperature $T(t)$ (K), pressure $p(t)$ (Pa), relative humidity $\text{RH}(t)$ (dimensionless), and dry density $\rho_{\text{dry}}(t)$ (kg m^{-3}). For the simulation in Section 5 the air temperature is prescribed as a function of time, while the air pressure and water mixing ratio are kept constant and the relative humidity and dry density are updated accordingly.

We assume that we are modeling a vertical slice of a well-mixed boundary layer during the day and a slice of the residual layer during the night, always surrounded to the sides

and above by background air. The height of the boundary layer is given by $H(t)$ (m). We denote by $\lambda_{\text{dil,horiz}}(t)$ (s^{-1}) the horizontal dilution rate with the prescribed background gas and aerosol, and by $\lambda_{\text{dil,vert}}(t)$ (s^{-1}) the vertical dilution rate that represents entrainment of a growing boundary layer. The total dilution rate $\lambda_{\text{dil}}^{\text{eff}}(t)$ (s^{-1}) is then given by

$$\lambda_{\text{dil}}(t) = \lambda_{\text{dil,horiz}}(t) + \lambda_{\text{dil,vert}}(t) \quad (2)$$

$$\lambda_{\text{dil,vert}} = I_{\text{entrain}}(t) \max\left(0, \frac{1}{H(t)} \frac{dH(t)}{dt}\right), \quad (3)$$

where vertical entrainment only occurs for increasing boundary layer heights. The indicator $I_{\text{entrain}}(t)$ is 1 when the modeled air parcel is within the boundary layer and so entrainment is possible, and is 0 when the air parcel is in the residual layer.

To obtain the mean evolution in the large-number limit we neglect correlations between the number of particles of different sizes [Gillespie, 1972] and thus obtain the classical Smoluchowski coagulation equation [von Smoluchowski, 1916a, b], which for a multidimensional aerosol distribution with gas coupling is

$$\frac{\partial n(\vec{\mu}, t)}{\partial t} = \frac{1}{2} \int_0^{\mu_1} \int_0^{\mu_2} \dots \int_0^{\mu_A} K(\vec{\mu}', \vec{\mu} - \vec{\mu}') \times n(\vec{\mu}', t) n(\vec{\mu} - \vec{\mu}', t) d\mu'_1 d\mu'_2 \dots d\mu'_A \quad (4a)$$

$$- \int_0^{\infty} \int_0^{\infty} \dots \int_0^{\infty} K(\vec{\mu}, \vec{\mu}') \times n(\vec{\mu}, t) n(\vec{\mu}', t) d\mu'_1 d\mu'_2 \dots d\mu'_A \quad (4b)$$

$$+ \dot{n}_{\text{emit}}(\vec{\mu}, t) \quad (4c)$$

$$+ \lambda_{\text{dil}}(t) (n_{\text{back}}(\vec{\mu}, t) - n(\vec{\mu}, t)) \quad (4d)$$

$$- \sum_{i=1}^C \frac{\partial}{\partial \mu_i} \left(c_i I_i(\vec{\mu}, \vec{g}, t) n(\vec{\mu}, t) \right) \quad (4e)$$

$$- \frac{\partial}{\partial \mu_{C+1}} \left(c_w I_w(\vec{\mu}, \vec{g}, t) n(\vec{\mu}, t) \right) \quad (4f)$$

$$+ \frac{1}{\rho_{\text{dry}}(t)} \frac{d\rho_{\text{dry}}(t)}{dt} n(\vec{\mu}, t) \quad (4g)$$

$$\frac{dg_i(t)}{dt} = \dot{g}_{\text{emit},i}(t) + \lambda_{\text{dil}}(t) (g_{\text{back},i}(t) - g_i(t)) \quad (4h)$$

$$+ R_i(\vec{g}) \quad (4i)$$

$$- \int_0^{\infty} \int_0^{\infty} \dots \int_0^{\infty} I_i(\vec{\mu}, \vec{g}, t) \times n(\vec{\mu}, t) d\mu_1 d\mu_2 \dots d\mu_A \quad (4j)$$

$$+ \frac{1}{\rho_{\text{dry}}(t)} \frac{d\rho_{\text{dry}}(t)}{dt} g_i(t). \quad (4k)$$

The integro-differential equation (4) must be augmented with appropriate boundary conditions. This is done on physical grounds to ensure that the constituent masses of particles cannot become negative. In equation (4), $K(\vec{\mu}_1, \vec{\mu}_2)$ ($\text{m}^3 \text{s}^{-1}$) is the coagulation rate between particles with constituent masses $\vec{\mu}_1$ and $\vec{\mu}_2$, $\dot{n}_{\text{emit}}(\vec{\mu}, t)$ ($\text{m}^{-3} \text{kg}^{-A} \text{s}^{-1}$) is the number distribution rate of aerosol emissions, $n_{\text{back}}(\vec{\mu}, t)$ ($\text{m}^{-3} \text{kg}^{-A}$) is the background number distribution, $I_i(\vec{\mu}, \vec{g}, t)$ (mol s^{-1}) is the condensation or evaporation flux of gas species i (with $I_w(\vec{\mu}, \vec{g}, t)$ the flux for water), c_i ($\text{m}^3 \text{mol}^{-1}$) is the conversion factor from moles of gas species i to mass of aerosol species i (with c_w the factor for water), $\dot{g}_{\text{emit},i}(t)$ ($\text{mol m}^{-3} \text{s}^{-1}$) is the emission rate of gas species i , $g_{\text{back},i}(t)$ (mol m^{-3}) is the background concentration of gas species i , and $R_i(\vec{g})$ ($\text{mol m}^{-3} \text{s}^{-1}$) is the concentration growth rate of gas species i due to gas chemical reactions. Many of the rates, coefficients and functions

also depend on the environmental conditions, but we have not written this dependence explicitly.

3. Particle-resolved aerosol models

3.1. PartMC aerosol state representation

We consider a Lagrangian parcel with volume V (m^3), also called the computational volume. We represent the aerosol state by storing N_{MC} particles in this volume, written $\Pi = (\vec{\mu}^1, \vec{\mu}^2, \dots, \vec{\mu}^{N_{\text{MC}}})$, where the particle order is not significant. Each particle is an A -dimensional vector $\vec{\mu}^i \in \mathbb{R}^A$ with components $(\mu_1^i, \mu_2^i, \dots, \mu_A^i)$, so μ_a^i is the mass of species a in particle i , for $a = 1, \dots, A$ and $i = 1, \dots, N_{\text{MC}}$. In the notation of Debyr *et al.* [2003] for the Mass Flow Algorithm, we are taking $(\omega_i/y_i)(t) = 1$, which means one computational particle per physical particle. While we track every particle within the computational volume V , we regard this volume as being representative of a much larger air parcel. For example, in Section 5 we use a computational volume on the order of a few cubic centimeters but take this to be approximating the state of the well-mixed boundary layer during the day and the residual layer during the night.

The simulation of the aerosol state proceeds by two mechanisms. First, the composition of each particle can change, changing the components of the vector $\vec{\mu}^i$ as species condense from the gas phase and evaporate to it, for example. Second, the population Π can have particles added and removed, either by emissions, dilution or coagulation events between particles.

The representation of the aerosol as a finite collection of particles Π in a volume V is very flexible, as other properties can easily be stored for each particle, such as fractal dimension, electric charge, age since emission, etc. In the present paper we store the number of coagulation events undergone by each particle to produce Figure 15.

3.2. PartMC emissions

Because we are using a finite number of particles to approximate the current aerosol population, we need to add a finite number of emitted particles to the volume at each timestep. Over time these finite particle samplings should approximate the continuum emission distribution, so the samplings at each timestep must be different. We assume that emissions are memoryless, so that emission of each particle is uncorrelated with emission of any other particle. Under this assumption the appropriate statistics are Poisson distributed, whereby the distribution of finite particles is parametrized by the mean emission rate and distribution.

Consider a number distribution production rate $\dot{n}_{\text{emit}}(\vec{\mu}, t)$ ($\text{m}^{-3} \text{kg}^{-A} \text{s}^{-1}$), a volume V (m^3), and a timestep Δt (s). The emissions over the timestep from time t_0 to $t_1 = t_0 + \Delta t$ are given by

$$n_{\text{emit}}(\vec{\mu}; t_0, t_1) = \int_{t_0}^{t_1} \dot{n}_{\text{emit}}(\vec{\mu}, t) dt \quad (5)$$

$$\approx (t_1 - t_0) \dot{n}_{\text{emit}}(\vec{\mu}, t_0) \quad (6)$$

for which we use the first-order approximation above. To obtain a finite Poisson sample of the distribution $n(\vec{\mu}) = n_{\text{emit}}(\vec{\mu}; t_0, t_1)$ ($\text{m}^{-3} \text{kg}^{-A}$) in the computational volume V we first see that the mean number $N(n, V)$ of sampled particles will be

$$N_{\text{mean}}(n, V) = \int_0^{\infty} \int_0^{\infty} \dots \int_0^{\infty} n(\vec{\mu}) V d\mu_1 d\mu_2 \dots d\mu_A. \quad (7)$$

The actual number S of emitted particles added in a timestep will be Poisson distributed, written $S \sim \text{Pois}(\lambda)$, for mean $\lambda = N_{\text{mean}}(n, V)$, so that

$$\text{Prob}(S = k) = \frac{\lambda^k e^{-\lambda}}{k!} \text{ for } k \in \mathbb{Z}^+. \quad (8)$$

A Poisson sampling Π_{samp} of the number distribution $n(\vec{\mu})$ in volume V , written $\Pi_{\text{samp}} \sim \text{Pois}_{\text{dist}}(n, V)$, is a finite sequence of particles given by

$$\Pi_{\text{samp}} = (\vec{\mu}^1, \vec{\mu}^2, \dots, \vec{\mu}^S) \quad (9a)$$

$$S \sim \text{Pois}(N_{\text{mean}}(n, V)) \quad (9b)$$

$$\vec{\mu}^s \sim \frac{n(\vec{\mu})V}{N_{\text{mean}}(n, V)} \text{ for } s = 1, \dots, S, \quad (9c)$$

where (9c) means that each particle has a composition drawn from the distribution specified by $n(\vec{\mu})$.

3.3. PartMC dilution

As with emissions, we must also obtain a finite sampling of background particles that have diluted into our computational volume during each timestep. In addition, some of the particles in our current sample will dilute out of our volume and will be lost, so this must be sampled as well. We assume that dilution is memoryless, so that dilution of each particle is uncorrelated with the dilution of any other particle or itself at other times, and that once a particle dilutes out it is no more likely to re-enter than any other background particle.

Let the background particle distribution be $n_{\text{back}}(\vec{\mu}, t)$ ($\text{m}^{-3} \text{kg}^{-A}$), the computational volume be V (m^3), and the timestep be Δt (s). The distribution of particles that dilute from the background into the volume V between times t_0 and $t_1 = t_0 + \Delta t$ is $n_{\text{dil}}(\vec{\mu}; t_0, t_1)$, where $n_{\text{dil}}(\vec{\mu}; t_0, t)$ satisfies

$$\frac{\partial n_{\text{dil}}(\vec{\mu}; t_0, t)}{\partial t} = \lambda_{\text{dil}}(t) (n_{\text{back}}(\vec{\mu}, t) - n_{\text{dil}}(\vec{\mu}; t_0, t)) \quad (10a)$$

$$n_{\text{dil}}(\vec{\mu}; t_0, t_0) = 0 \quad (10b)$$

We use the first-order approximation given by

$$n_{\text{dil}}(\vec{\mu}; t_0, t_1) \approx (t_1 - t_0) \lambda_{\text{dil}}(t_0) n_{\text{back}}(\vec{\mu}, t_0) \quad (11)$$

A discrete sampling of $n_{\text{dil}}(\vec{\mu}; t_0, t_1)$ is then given by $\Pi_{\text{dil}} \sim \text{Pois}_{\text{dist}}(n_{\text{dil}}(\vec{\mu}), V)$, as in (9).

If we start the timestep at time t_0 with the particle population Π , then each particle in Π has probability $p(t_0, t_1)$ to be lost by dilution during the timestep, where $p(t_0, t)$ satisfies

$$\frac{\partial p(t_0, t)}{\partial t} = \lambda_{\text{dil}}(t) (1 - p(t_0, t)) \quad (12a)$$

$$p(t_0, t_0) = 0 \quad (12b)$$

We use the first-order approximation given by

$$p(t_0, t_1) \approx (t_1 - t_0) \lambda_{\text{dil}}(t_0) \quad (13)$$

We denote the binomial distribution for number n and probability p by $B(n, p)$. The number of particles lost from Π between times t_0 and $t_1 = t_0 + \Delta t$ is then given by N_{loss} which is distributed as

$$N_{\text{loss}} \sim B(N_{\text{MC}}, p(t_0, t_1)) \quad (14)$$

$$\approx \text{Pois}(N_{\text{MC}} p(t_0, t_1)) \quad (15)$$

We approximate the binomial distribution with a Poisson distribution as above, which converges as $\Delta t \rightarrow 0$ for fixed N_{MC} . As each particle has equal probability to be lost due to dilution, we can sample N_{loss} and then choose N_{loss} particles uniformly from Π to be removed.

3.4. Coupled PartMC-MOSAIC method

We couple the stochastic PartMC particle-resolved aerosol model to the deterministic MOSAIC gas- and aerosol-chemistry code in a time-splitting fashion to obtain a complete discretization of the governing equations (4). The aerosol distribution $n(\vec{\mu}, t)$ is represented by N_{MC} particles in a computational volume V , as described above, while the gas vector $\vec{g}(t)$ stores the gas concentrations. Equations (4a)–(4d) are solved stochastically by the PartMC code, and the gas equations (4h)–(4j) together with the coupling term (4e) are integrated deterministically by the MOSAIC code. The terms (4g) and (4k) are implemented deterministically by updating V and \vec{g} by the density change or its inverse, as appropriate. The full coupled PartMC-MOSAIC algorithm is given in Figure 1.

The current version of MOSAIC treats all the locally and globally important aerosol species including SO_4 , NO_3 , Cl, CO_3 , MSA (methanesulfonic acid), NH_4 , Na, Ca, other inorganic mass, BC, and POM, and secondary organic mass. It consists of four computationally efficient modules: 1) the gas-phase photochemical mechanism CBM-Z [Zaveri and Peters, 1999]; 2) the Multicomponent Taylor Expansion Method (MTEM) for estimating activity coefficients of electrolytes and ions in aqueous solutions [Zaveri et al., 2005b]; 3) the Multicomponent Equilibrium Solver for Aerosols (MESA) for intra-particle solid-liquid partitioning [Zaveri et al., 2005a]; and 4) the Adaptive Step Time-split Euler Method (ASTEM) for dynamic gas-particle partitioning over size- and composition-resolved aerosol [Zaveri et al., 2008]. The version of MOSAIC box-model implemented here also includes a treatment for secondary organic aerosol (SOA) based on the SORGAM scheme [Schell et al., 2001].

Π is the sequence of particle compositions
 V is the computational volume
 \vec{g} is the gas concentrations
 $t = 0$
while $t < t_{\text{final}}$ **do**:
 $t = t + \Delta t$
 update temperature $T(t)$, pressure $p(t)$, relative humidity $RH(t)$, dry density $\rho_{\text{dry}}(t)$, and mixing height $H(t)$
 $V(t) = V(t - \Delta t) \frac{\rho_{\text{dry}}(t - \Delta t)}{\rho_{\text{dry}}(t)}$
 $\vec{g}(t) = \vec{g}(t - \Delta t) \frac{\rho_{\text{dry}}(t)}{\rho_{\text{dry}}(t - \Delta t)}$
 add $\Delta t \dot{\vec{g}}_{\text{emit}}(t) + \Delta t \lambda_{\text{dil}}(t) (\vec{g}_{\text{back}}(t) - \vec{g}(t))$ to \vec{g}
 randomly choose $N_{\text{loss}} \sim \text{Pois}(\Delta t \lambda_{\text{dil}} N_{\text{MC}})$ and remove N_{loss} randomly chosen particles from Π
 add a sample of $\text{Pois}_{\text{dist}}(\lambda_{\text{dil}} \Delta t n_{\text{back}}(\cdot, t), V)$ to Π
 add a sample of $\text{Pois}_{\text{dist}}(\Delta t \dot{n}_{\text{emit}}(\cdot, t), V)$ to Π
 perform one Δt -timestep of coagulation for Π with the PartMC algorithm in Figure 2
 integrate the system of coupled ODEs (4e) and (4i)–(4j) with MOSAIC for time Δt
end while

Figure 1. Coupled PartMC-MOSAIC algorithm.

4. PartMC coagulation algorithm

4.1. Stochastic coagulation simulation

If we have N_{MC} particles then there are $N_{\text{MC}}(N_{\text{MC}} - 1)/2$ possible coagulation events, with the probability rate of a coagulation between particles i and j in a volume V given by $K(\vec{\mu}^i, \vec{\mu}^j)/V$ for the coagulation kernel $K(\vec{\mu}^i, \vec{\mu}^j)$ ($\text{m}^3 \text{s}^{-1}$). The only difficulty with stochastic coagulation is generating a sequence of coagulation events, each consisting of a pair of particles (i, j) that coagulate and a time Δt until the coagulation occurs. Once a coagulation event is determined then we simply remove the particles i and j from the population Π , add a new particle with composition $\vec{\mu}^{\text{new}} = \vec{\mu}^i + \vec{\mu}^j$, and advance the time by Δt .

The standard stochastic simulation algorithm for this system is due to Gillespie [1975] and is based on the observation that the probability density for the time until the next coagulation event is

$$P(\Delta t) = \frac{K_{\text{tot}}}{V} e^{-K_{\text{tot}}\Delta t/V}, \quad (16)$$

where $K_{\text{tot}} = \sum_{i < j} K(\vec{\mu}^i, \vec{\mu}^j)$ is the total rate. We can thus generate an elapsed time by sampling the probability density function (16). The conditional probability that the coagulation event that occurred was between particles i and j is then

$$P(i, j | \Delta t) = \frac{K(\vec{\mu}^i, \vec{\mu}^j)}{K_{\text{tot}}}, \quad (17)$$

and this can be sampled to determine which particles coagulated, and then the coagulation event can be performed.

Gillespie's method has the advantage that it generates exact realizations of the stochastic coagulation process. It faces two main difficulties in practice, however. First, the total rate K_{tot} continually changes as coagulation events occur and particle compositions change due to condensation. Computing a reasonable estimate of this parameter quickly becomes exceedingly expensive, and approximations made to speed up this estimate introduce errors that are difficult to estimate and control. Second, while sampling (16) is very cheap, sampling (17) can be expensive for complex kernels. The two main methods are use of the cumulative distribution function, which scales badly in the number of particles and is thus too expensive for large particle numbers, and use of accept-reject. While accept-reject scales well as the number of particles grows, it is very inefficient if the kernel K_{ij} is highly non-uniform, as is unfortunately the case for many physically relevant aerosol distributions. Despite these difficulties, Gillespie's method is by far the most commonly used method in practice, with many slight variants appearing in the literature (for example, see *Efendiev and Zachariah* [2002]; *Kruis et al.* [2000]; *Garcia et al.* [1987]; *Fichthorn and Weinberg* [1991]).

To avoid these two difficulties we formulate an improved method. We use a fixed timestep method and we develop a binned acceptance procedure. The use of a fixed timestep removes the need to know K_{tot} , albeit with the introduction of some error. This fixed timestep also makes it easy to integrate the coagulation with other physics and chemistry using a time-splitting scheme. The binned sampling method means that we are not subject to slow-downs from non-uniform kernels.

4.2. Fixed-timestep stochastic coagulation

We choose a fixed timestep Δt and in each timestep choose N_{test} particle pairs to test. We then generate N_{test} random particle pairs uniformly and for each pair (i, j) we accept a coagulation event with probability

$$P(i, j) = 1 - \exp\left(\frac{-K(\vec{\mu}^i, \vec{\mu}^j)\Delta t}{V} \frac{N_{\text{MC}}(N_{\text{MC}} - 1)}{N_{\text{test}}}\right) \approx \frac{K(\vec{\mu}^i, \vec{\mu}^j)\Delta t}{V} \frac{N_{\text{MC}}(N_{\text{MC}} - 1)}{N_{\text{test}}}. \quad (18)$$

In the limit $\Delta t \rightarrow 0$ this generates an exact realization of the stochastic coagulation process, and for finite Δt introduces a discretization error. The number N_{test} should be chosen large enough that $P(i, j) \leq 1$ for all pairs i, j and for convergence it must remain bounded away from zero as $\Delta t \rightarrow 0$. This is similar to the sampling technique used in *Debry et al.* [2003].

The efficiency of the method, as with any procedure of accept-reject type, is greatest when the maximum value of $P(i, j)$ is as close as possible to 1. To ensure this we choose

$$N_{\text{test}} = \left\lceil K_{\text{max}}\Delta t N_{\text{MC}}(N_{\text{MC}} - 1)/V \right\rceil, \quad (19)$$

where $K_{\text{max}} = \max_{i, j} K(\vec{\mu}^i, \vec{\mu}^j)$ is the maximum kernel value and $\lceil x \rceil$ is the least integer greater than x . In practice we take K_{max} to be a cheaply computable upper-bound for $K(\vec{\mu}^i, \vec{\mu}^j)$, which slightly increases the accuracy of the method and is much cheaper.

The fixed timestep method thus cleanly resolves the difficulties with Gillespie's method to do with the need to determine K_{tot} . It still has the problem, however, that if the kernel $K(\vec{\mu}^i, \vec{\mu}^j)$ is very non-uniform then the acceptance procedure will be very inefficient. To fix this, we adopt a binned approach.

4.3. Binned stochastic coagulation

For coagulation kernels of physical interest, such as those arising from Brownian motion or gravitational settling, the kernel $K(\vec{\mu}, \vec{\mu}')$ is highly multiscale, with many orders of magnitude difference between the highest and lowest rates. This is a problem for the sampling procedure outlined in the previous section, because N_{test} will be very large and so we will have to reject many events using (18) for each accepted event.

To accelerate this procedure we take advantage of the fact that the kernel $K(\vec{\mu}^i, \vec{\mu}^j)$ is not random in its non-uniformity, but rather depends primarily on the diameter of the particles. This means that if pairs i, j and k, ℓ are

divide diameter axis into bins as for a sectional model
 $N_{\text{MC}}(b)$ is the number of particles in bin b
 $\vec{\mu}(b, i)$ is the mass vector of the i -th particle in bin b
 $K_{\text{max}}(b_1, b_2)$ is a precomputed upper bound on the kernel for any particles from bins b_1 and b_2
 Δt is the timestep
for all bin pairs (b_1, b_2) do:
 $N_{\text{event}} = N_{\text{MC}}(b_1)N_{\text{MC}}(b_2)/2$
 $N_{\text{test}} = \left\lceil K_{\text{max}}(b_1, b_2)\Delta t N_{\text{event}}/V \right\rceil$
for N_{test} repetitions do:
 randomly choose particles i_1 and i_2 uniformly in bins b_1 and b_2
 $K_{12} = K(\vec{\mu}(b_1, i_1), \vec{\mu}(b_2, i_2))$
 randomly choose r uniformly in $[0, 1]$
if $r < K_{12}\Delta t N_{\text{event}}/(N_{\text{test}}V)$ then:
 coagulate the two particles, updating the arrays $N(b)$ and $\vec{\mu}(b, i)$
end if
end for
end for

Figure 2. PartMC coagulation algorithm.

similar, so that the diameters of particles i and k are close, as are the diameters of particles j and ℓ , then $K(\bar{\mu}^i, \bar{\mu}^j) \approx K(\bar{\mu}^k, \bar{\mu}^\ell)$. We thus group particles into bins sorted by diameter and we use the acceptance procedure (18) for each pair of bins separately. This binned approach ensures that all particle pairs under consideration in a particular iteration have similar coagulation rates, and hence the procedure will have a high proportion of acceptances. Use of a binned version of the fixed timestep algorithm means that the number of samples (19) done per pair of bins is automatically adapted to the number of particles in those bins. It also allows us to pre-compute the K_{\max} values for each bin pair. The resulting algorithm is shown in Figure 2.

The primary disadvantage of using a binned sampling procedure is in code complexity, as the bin structures of particles with similar sizes need to be constructed and maintained. This also adds a small amount of computational overhead to the coagulation routine, which is far outweighed by the enormous efficiency gains. We should note that the binned sampling procedure introduces no error in the simulation and is a pure efficiency gain. For typical aerosol profiles the binned procedure gives about two to four orders-of-magnitude speedup in computational time, as quantified in Section 4.4.

As a result of continuous coagulation the total number of simulated particles decreases with time. To maintain sufficient resolution and adequate statistics we double the number of particles whenever the number of particles becomes less than half of the original particle number. This corresponds to a doubling of the computational volume. When we include emissions of particles, the particle number eventually becomes too large and we run into computational limits. To avoid this we halve the number of particles when we have more than twice the original number of particles, which corresponds to a halving of the computational volume.

For some kernels, such as the Brownian kernel used in Section 5, the kernel is primarily dependent on the particle

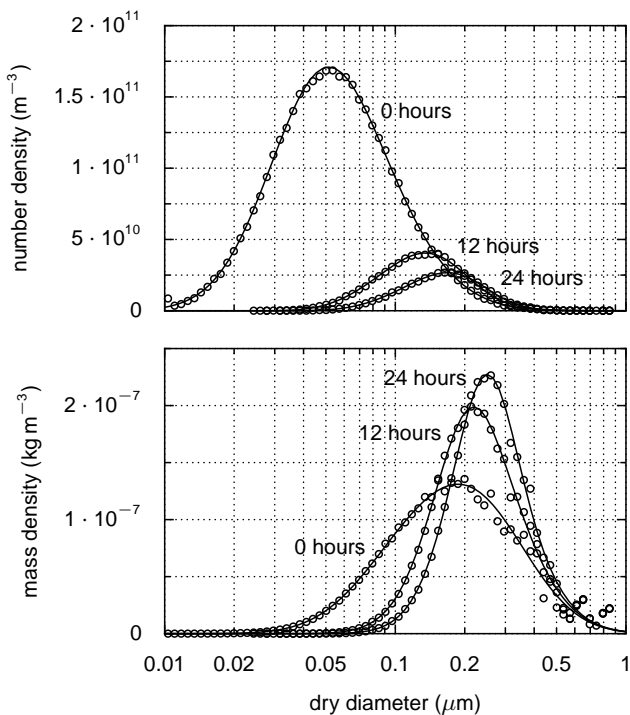


Figure 3. Comparison of the stochastic particle-resolved method using 10^5 particles (circles) against a sectional solution (lines) to the Smoluchowski equation for the Brownian kernel according to *Jacobson* [1999].

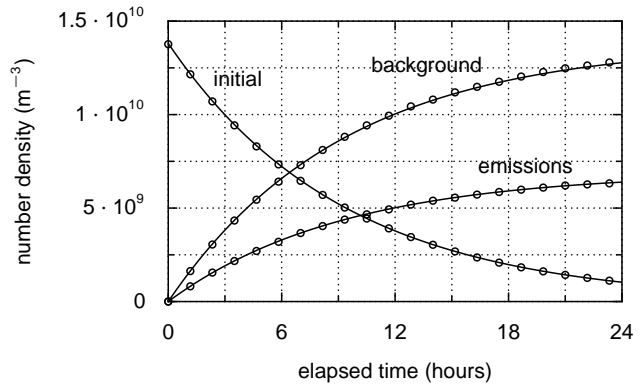


Figure 4. Comparison of the stochastic particle-resolved method using 10^5 particles (circles) against the analytical solution (lines) for a simulation with only constant mean rate emissions and dilution.

diameters but also depends on particle density. We could store the particles sorted into a 2D array per-diameter-bin and per-density-bin, but the density variation is bounded and small enough that it is still reasonably efficient to store them only per-diameter-bin and to compute K_{\max} to take the maximum density variation into account.

To enable efficient coagulation, the particle array Π is stored as an array of pointers to partially-filled particle arrays, one per diameter-bin. Insertions into bin arrays are performed at the end of the currently filled area and deletions from the middle are followed by a shift of the last element into the gap, ensuring full packing of each bin array at all times. Each diameter-bin array is reallocated to twice its existing size when necessary or half its existing size when possible. This gives constant-time random access at the cost of $O(\log \Delta N_{\text{MC}})$ reallocations and at most twice the minimal memory usage.

4.4. Verification of the PartMC coagulation algorithm

For verification of the PartMC stochastic coagulation method we compared PartMC using 10^5 particles against a sectional solution to the Smoluchowski equation [*Bott*, 1998] for a Brownian kernel [*Jacobson*, 1999]. For Figure 3 we used two overlapping log-normal modes as the initial condition and the results show that we have excellent agreement for the number and mass distributions for this test case, which is representative of the simulation in Section 5. At the very largest sizes there is some noise in the particle-based mass distribution, as each individual particle has significant mass at these sizes. This noise could be reduced by averaging several simulations in a Monte Carlo fashion, or by using a variable number of physical particles per computational particle, as in the Mass Flow Algorithm [*Babovsky*, 1999; *Eibeck and Wagner*, 2001]. We do not consider this noise to be significant enough for the study in this paper to require amelioration.

For the Brownian kernel in Figure 3 the use of the binned stochastic coagulation algorithm of Section 4.3 improved the accept rate from 0.95% to 86%, requiring more than 90 times fewer kernel evaluations. For a more non-uniform gravitational kernel, such as found in cloud-aerosol simulations, the binned algorithm increased the accept rate from 0.007% to 86%, a reduction of over 12,000 times in the number of kernel evaluations (not shown in a figure).

Figure 4 compares the stochastic treatment of emissions and dilution using 10^5 particles against the analytical solution for constant mean emission and dilution rates. This test also shows excellent agreement. We thus see that PartMC-MOSAIC is performing emissions, dilution, and coagulation accurately, and the chemistry modeling is of similar accuracy to that in current state-of-the-art sectional and modal aerosol models.

Table 1. Initial concentrations of gas phase species and average gas phase emissions. The emissions represent area emissions and are averaged over the 12-hour emission period. We obtain the volume emission rate $\bar{g}_{\text{emit}}(t)$ in equation (4h) by dividing by the mixing height $H(t)$.

MOSAIC species	Concentration in ppb	Emissions in nmol m ⁻² s ⁻¹
NO	0.1	31.8
NO ₂	1.0	1.67
HNO ₃	1.0	-
O ₃	50.0	-
H ₂ O ₂	1.1	-
CO	21	291.3
SO ₂	0.8	2.51
NH ₃	0.5	6.11
HCl	0.7	-
CH ₄	2200	-
C ₂ H ₆	1.0	-
HCHO	1.2	1.68
CH ₃ OH	0.12	0.28
CH ₃ OOH	0.5	-
ALD2	1.0	0.68
PAR	2.0	96
AONE	1.0	1.23
ETH	0.2	7.2
OLET	$2.3 \cdot 10^{-2}$	2.42
OLEI	$3.1 \cdot 10^{-4}$	2.42
TOL	0.1	4.04
XYL	0.1	2.41
ONIT	0.1	-
PAN	0.8	-
RCOOH	0.2	-
ROOH	$2.5 \cdot 10^{-2}$	-
ISOP	0.5	0.23
ANOL	-	3.45

Table 2. Initial and emitted aerosol distribution parameters, as in equation (23). The initial aerosol distribution is also used as the background aerosol distribution. E is the area source strength of particle emissions. Dividing E by the mixing height $H(t)$ and multiplying by a normalized composition distribution gives the number distribution emission rate $\dot{n}_{\text{emit}}(\bar{\mu}, t)$ in equation (4c).

	N in m ⁻³	D_{gn} in μm	σ_{g}	Composition
Initial mode 1	$3.2 \cdot 10^9$	0.02	1.45	50% (NH ₄) ₂ SO ₄ , 50% POM
Initial mode 2	$2.9 \cdot 10^9$	0.116	1.65	50% (NH ₄) ₂ SO ₄ , 50% POM
	E in m ⁻² s ⁻¹	D_{gn} in μm	σ_{g}	Composition
Meat cooking	$9 \cdot 10^6$	0.086	1.9	POM
Diesel vehicles	$1.6 \cdot 10^8$	0.05	1.7	10% POM, 90% BC
Gasoline vehicles	$5 \cdot 10^7$	0.05	1.7	66% POM, 34% BC

5. Application of PartMC-MOSAIC to an idealized urban plume scenario

5.1. Setup of case study

For this study we considered an idealized urban plume scenario. We tracked the evolution of gas phase species and aerosol particles in a Lagrangian air parcel that initially contains background air and is advected over and beyond a large urban area. The simulation started at 06:00 local standard time (LST), and during the advection process, primary trace gases and aerosol particles from different sources were emitted into the air parcel for 12 hours. After 18:00 LST, the emissions were switched off, and the evolution of the air parcel was tracked for another 12 hours.

Initial gas-phase concentrations and emissions were adapted from the Southern California Air Quality Study (SCAQMS) simulation (August 26-29, 1988 period) in *Zaveri et al.* [2008], and are listed in Table 1. Note that while gas phase emissions in the simulation varied with time, Table 1 gives only the average over the emission period. The initial particle size distribution, which was identical to the background aerosol distribution, was bimodal with Aitken and accumulation modes [*Jaenicke*, 1993]. We assumed that it consisted of (NH₄)₂SO₄ and primary organic mass (see Table 2). We considered three different types of carbonaceous aerosol emissions: 1) meat cooking aerosol, 2) diesel vehi-

cle soot, and 3) gasoline vehicle soot. The parameters for the size distributions of these three emission categories were based on *Eldering and Cass* [1996], *Kittelson et al.* [2006a], and *Kittelson et al.* [2006b], respectively. The emission rates and the compositions were adapted from the California Air Resources Board database [*California Air Resources Board*, 2007].

For simplicity in this idealized study, the particle emissions strength and their size and composition were kept constant with time. Furthermore, we assumed that the particles from these sources were emitted as fully-internal mixtures of the species listed in Table 2, since to date the mixing state of particle emissions is still not well characterized. Hence, it is difficult to justify a more sophisticated treatment for the emissions. However, once this data is available it will be straightforward to implement the information accordingly in our model. Sea salt, biomass burning and mineral dust particles as well as particles from biological sources (e.g. pollen) were not treated in this test case.

Before we discuss the results on aerosol mixing state in detail we provide the context for the conditions in our case study with Figures 5 to 8. We did not attempt to simulate a specific episode or trajectory for the Los Angeles basin (as was done in *Kleeman et al.* [1997]), but rather an idealized urban plume scenario, with conditions that were consistent with a polluted environment. The temperature,

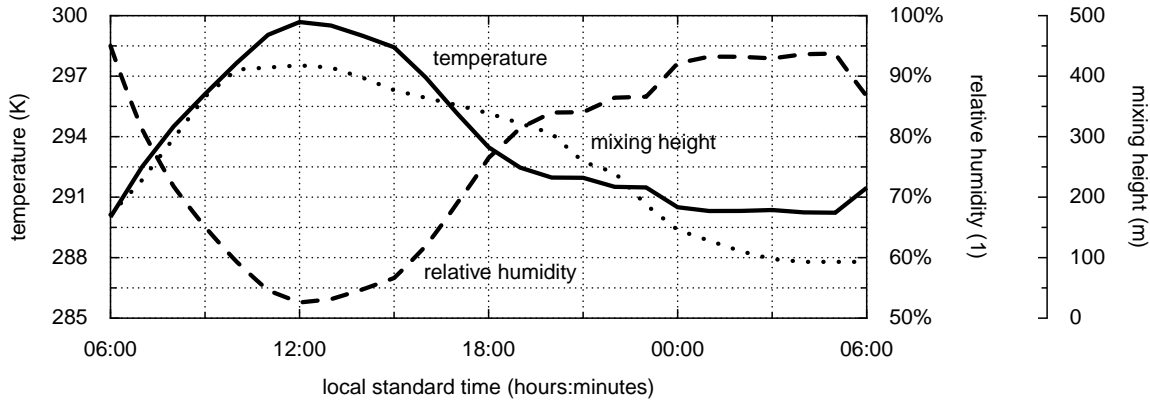


Figure 5. Time series of temperature, relative humidity, and mixing height over the course of the 24-hour simulation.

relative humidity, and mixing height along the trajectory were adapted from spatially-averaged values from the Los Angeles Air Basin simulation of Zaveri *et al.* [2008] and references therein. The temperature and mixing height were prescribed as functions of time, while the pressure and water mixing ratio were kept constant and the relative humidity and dry density were updated accordingly. The variation of these parameters is shown in Figure 5. The relative humidity started at 95%, then decreased to 53% during the day and increased again to 94% during the following night. As we show below, the diurnal cycle of the ambient conditions impacted the thermodynamic equilibria and the phase states of the particles.

An increase of the mixing height during the morning caused dilution of the gas and aerosol concentrations within the air parcel and was accompanied by entrainment of background air, as discussed in Section 3.2. We also considered dilution due to horizontal turbulent diffusion, using a first-order dilution rate of $1.5 \cdot 10^{-5} \text{ m s}^{-1}$.

We resolved the total aerosol distribution with 10^5 Monte Carlo particles initially. The corresponding initial total number density was $N = 6.1 \cdot 10^9 \text{ m}^{-3}$ and so the computational volume was initially $V = N_{\text{MC}}/N = 16 \text{ cm}^3$. It remained between $V = 8 \text{ cm}^3$ and $V = 17 \text{ cm}^3$ for the duration of the run as particle number N_{MC} and number density N changed due to emissions, dilution, and coagulation. The number of particles remained between $N_{\text{MC}} = 199799$ and $N_{\text{MC}} = 60655$. The timestep used for this simulation was $\Delta t = 1$ minute. While better estimates of the system statistics could be obtained with multiple realizations, we found a single run to give reasonable results in this case, as demonstrated in Figures 3 and 4 and discussed in Section 4.4. Although not shown here, runs with different random initialization gave essentially the same results.

To quantify the impact of coagulation we performed two runs, one base case including coagulation as described above,

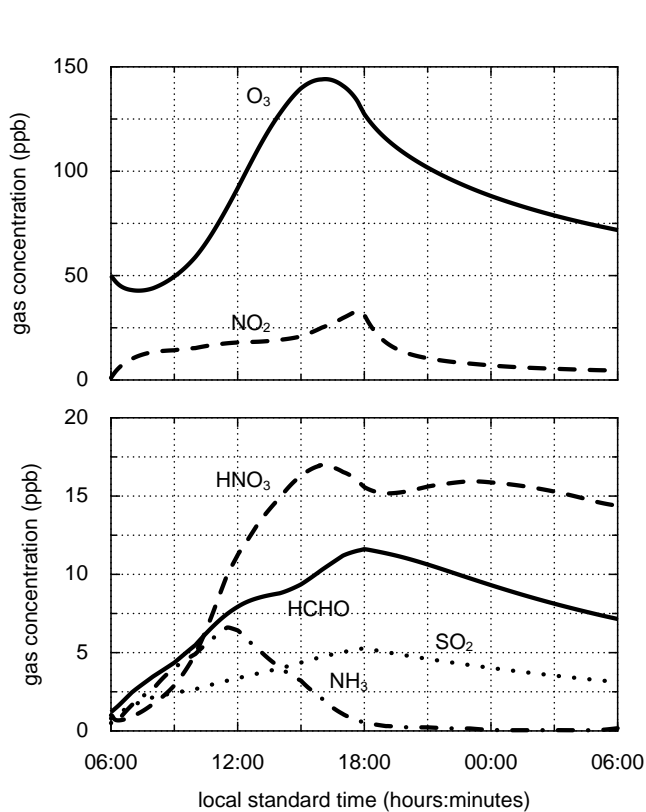


Figure 6. Time series of selected gas phase species.

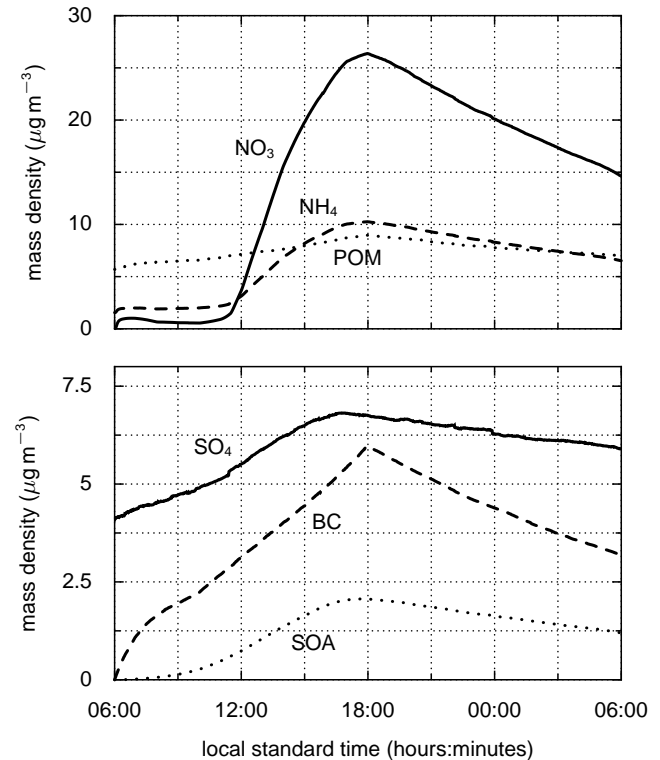


Figure 7. Time series of total mass densities of selected aerosol species: M_{NO_3} , M_{NH_4} , M_{POM} , M_{SO_4} , M_{BC} , and M_{SOA} .

and one case without coagulation. Otherwise, the conditions for the two runs were identical.

5.2. Gas species evolution

Figure 6 shows the evolution of selected gas phase species undergoing a diurnal cycle typical for a photochemistry episode under polluted conditions. During the daytime we observed a considerable production of O_3 , reaching a maximum value of 144 ppb at 16:09 LST. The NO_2 concentration increased up to 33 ppb during the time that NO_x was emitted, and decreased after 18:00 LST due to dilution and chemical reactions after the emissions had stopped. HNO_3 reached 17 ppb and contributed to the formation of ammonium nitrate in the particle phase. NH_3 levels reached 6.6 ppb during the daytime and later vanished due to gas-to-particle conversion. $HCHO$ was both emitted and chemically produced with a maximum value of 12 ppb at 17:59 LST.

5.3. Bulk aerosol evolution

Figure 7 shows time series of the bulk aerosol concentrations. We observe a pronounced production of ammonium nitrate, reaching nitrate concentrations of up to $26 \mu g m^{-3}$ and ammonium concentration of $10.3 \mu g m^{-3}$ in the late afternoon. Sulfate concentrations increased from $4.1 \mu g m^{-3}$ to $6.8 \mu g m^{-3}$ due to condensation of photochemically produced sulfuric acid. POM and BC were directly emitted and accumulated to $9.0 \mu g m^{-3}$ and $6.0 \mu g m^{-3}$, respectively, until 18:00 LST when the emissions stopped. After 18:00 LST the mass densities declined due to dilution, especially nitrate and BC for which the background concentration was zero.

5.4. Aerosol distribution functions

We take $N(D)$ (m^{-3}) to be the cumulative number distribution, giving the number of particles per volume that have diameter less than D . Similarly, the cumulative mass distribution $M(D)$ ($kg m^{-3}$) gives the mass per volume of particles with diameter less than D , while the per-species cumulative mass distribution $M_x(D)$ gives the mass per volume of species x in particles with diameter less than D . We write $N = N(\infty)$, $M = M(\infty)$, and $M_x = M_x(\infty)$ for the number, mass, and per-species mass densities, respectively.

Given the cumulative densities, we define the number distribution $n(D)$ (m^{-3}), mass distribution $m(D)$ ($kg m^{-3}$) and per-species mass distribution $m_x(D)$ ($kg m^{-3}$) by

$$n(D) = \frac{dN(D)}{d \log_{10} D} \quad (20)$$

$$m(D) = \frac{dM(D)}{d \log_{10} D} \quad (21)$$

$$m_x(D) = \frac{dM_x(D)}{d \log_{10} D}. \quad (22)$$

The initial, background, and emitted number densities used in this paper will all be superpositions of log-normal distributions, each defined by

$$n(D) = \frac{N}{\sqrt{2\pi} \log_{10} \sigma_g} \exp\left(-\frac{(\log_{10} D - \log_{10} D_{gn})^2}{2(\log_{10} \sigma_g)^2}\right) \quad (23)$$

where N (m^{-3}) is the total number density, D_{gn} (m) is the geometric mean diameter, and σ_g (dimensionless) is the geometric standard deviation.

To discuss the composition of a particle, we refer to certain mass fractions of species, as

$$f_{BC,POM} = \frac{\mu_{BC}}{\mu_{BC} + \mu_{POM}} \quad (24)$$

$$f_{BC,dry} = \frac{\mu_{BC}}{\mu_{dry}} \quad (25)$$

$$f_{H_2O,all} = \frac{\mu_{H_2O}}{\mu_{all}}, \quad (26)$$

where we recall that μ_x (m^3) is the mass of species x in a given particle, μ_{all} (m^3) is the total wet mass of the particle, and $\mu_{dry} = \mu_{all} - \mu_{H_2O}$ (m^3) is the total dry mass.

We extend the number and mass densities to be functions of both particle composition and diameter. That is, the two-dimensional cumulative number distribution $N_{y,x}(f, D)$ (m^{-3}) is the number of particles per volume that have a mass ratio of y to x less than f and a diameter less than D . The two-dimensional number distribution $n_{y,x}(f, D)$ (m^{-3}) is then defined by

$$n_{y,x}(f, D) = \frac{\partial^2 N_{y,x}(f, D)}{\partial f \partial \log_{10} D}. \quad (27)$$

The two-dimensional mass distribution $m_{y,x}(f, D)$ ($kg m^{-3}$) and cumulative mass distribution $M_{y,x}(f, D)$ ($kg m^{-3}$) are defined similarly.

We can also define two-dimensional densities based on other particle quantities. In particular, if we denote by k the number of coagulation events that a given particle has experienced during the simulation time then we can define the two-dimensional singly-cumulative number distribution $N_{coag}(k, D)$ (m^{-3}) to be the number of particles per volume with k coagulation events and diameter less than D . Then $n_{coag}(k, D)$ (m^{-3}) is defined by

$$n_{coag}(k, D) = \frac{\partial N_{coag}(k, D)}{\partial \log_{10} D}. \quad (28)$$

For ease of comparison between different plots we frequently use normalized densities denoted by a hat, so the normalized two-dimensional number distribution $\hat{n}_{y,x}(f, D)$ (dimensionless) is defined by

$$\hat{n}_{y,x}(f, D) = \frac{n_{y,x}(f, D)}{N}, \quad (29)$$

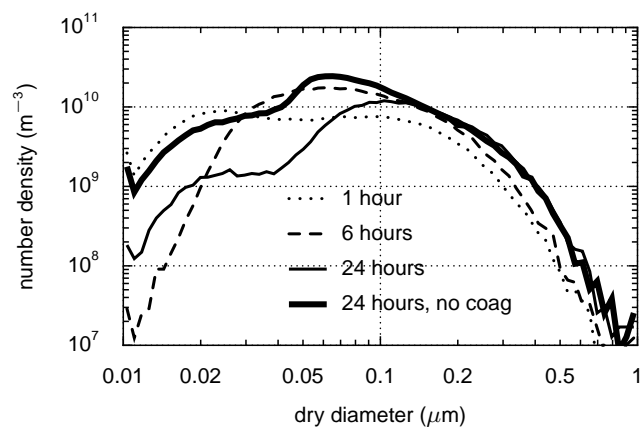


Figure 8. Number size distributions $n(D)$ for the simulation with coagulation after 1, 6, and 24 hours. For comparison the distribution without coagulation after 24 hours is also shown.

and similarly for the mass distribution.

We also find it convenient to plot one-dimensional mass densities for certain composition ranges, as done in Figure 14. We write $m_{\text{BC,dry}}([f_1, f_2], D)$ (kg m^{-3}) to refer to the total mass distribution (including water), where $f_{\text{BC,dry}}$ is between f_1 and f_2 ,

$$m_{\text{BC,dry}}([f_1, f_2], D) = M_{\text{BC,dry}}(f_2, D) - M_{\text{BC,dry}}(f_1, D). \quad (30)$$

5.5. Aerosol size distribution evolution

Figure 8 shows results of the number size distributions $n(D)$ after 1, 6, and 24 hours of simulation including coagulation. For comparison, the result after 24 hours of simulation without coagulation is also shown. The distribution after 1 hour still resembled the bimodal initial distribution (compare Table 2), which was identical to the background distribution. After 6 hours the distribution was primarily determined by the emissions. Concurrently, condensation of secondary species caused aerosol growth. Particles at small sizes were depleted due to coagulation. After 24 hours the Aitken mode of the background appeared again as a result of dilution. Compared to the size distribution without coagulation, the size distribution with coagulation showed a substantial decrease in number density for particles smaller than $0.1 \mu\text{m}$. With coagulation the total number density N peaked at the end of the emission period after 12 hours with a maximal value of $1.67 \cdot 10^{10} \text{ m}^{-3}$. After this, N declined due to coagulation and dilution to $7.36 \cdot 10^9 \text{ m}^{-3}$. The simulation without coagulation lead to a maximum total number density of $2.39 \cdot 10^{10} \text{ m}^{-3}$, and a final value of $1.54 \cdot 10^{10} \text{ m}^{-3}$. This means that coagulation decreased the peak and final total number concentrations by 30% and 52%, respectively. Comparing the number densities for the specific diameters $D = 0.03, 0.05, 0.07,$ and $0.1 \mu\text{m}$ with and without coagulation, we find that coagulation decreased the number density $n(D)$ by 82%, 84%, 66%, and 29% respectively.

We notice that for all size distributions shown in Figure 8 the results are somewhat “noisy” at small and large diameters. This noise is inherent to the stochastic model that is used for coagulation, dilution and emissions. Towards the edges of the size spectrum only a few particles are being used to represent the size distribution due to the low number density. Single particle variations arising from the stochastic model thus appear as a noisy curve. This could be rectified by averaging repeated Monte Carlo simulations or by using a variable number of physical particles per computational particle, as in the Mass Flow Algorithm [Babovsky, 1999; Eibeck and Wagner, 2001].

5.6. Aerosol mixing state evolution

While Figures 7 and 8 give an overview of aerosol size distribution and composition just like we obtain from traditional distribution-based models, they do not address the issue of mixing state. To elucidate how the mixing state evolved over the course of the simulation we display the data as shown in Figure 10. The panels show the two-dimensional number distributions as a function of dry size and mass fraction of BC, $f_{\text{BC,dry}}$, after 1, 5, 7, and 24 hours of simulation. This corresponds to LST 07:00, 11:00, 13:00, and 06:00 of the next morning. Our definition of the two-dimensional size distribution is described in Section 5.4 above.

We will discuss the evolution of the two-dimensional number size distribution in conjunction with Figure 11. The gray scale in this figure shows the water content of the particles, $f_{\text{H}_2\text{O,all}}$, as a function of BC mixing state, $f_{\text{BC,dry}}$, and particle size. We also include in Figure 9 the temporal evolution of the composition of three representative particles to aid the interpretation. These particles are labeled with P1, P2 and P3 in Figure 10.

Figure 10 shows the BC mixing state, $f_{\text{BC,dry}}$, relative to all other dry constituents. Since even at the time of emission no particles were pure BC, particles were not present

at $f_{\text{BC,dry}} = 100\%$. Fresh emissions from diesel vehicles ($f_{\text{BC,dry}} = 90\%$) and gasoline vehicles ($f_{\text{BC,dry}} = 34\%$) appear as horizontal lines since particles in one emission category were all emitted with the same composition. At $f_{\text{BC,dry}} = 0\%$ all the particles appear that do not contain any BC (i.e. background particles and particles from meat cooking emissions that have not undergone coagulation with particles containing BC). After 1 hour (07:00 LST) a small number of particles in between these three classes indicate the occurrence of coagulation.

Under the initial ambient conditions the emitted diesel and gasoline particles accumulated small amounts of ammonium sulfate, ammonium nitrate and water. After 06:44 LST the relative humidity fell below 85%, which is the deliquescence point of the inorganic mixture of ammonium, sulfate and nitrate. As a result of the hysteresis of particle deliquescence and crystallization, the particles that had been emitted up to this point stayed wet throughout the

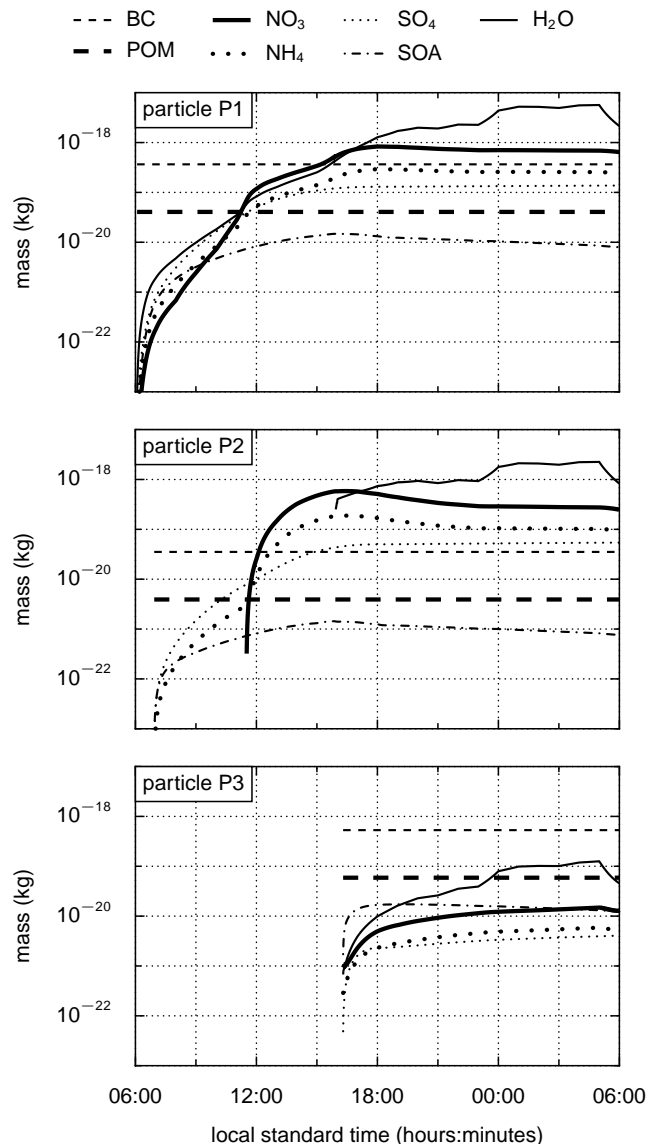


Figure 9. Time history of the composition of three individual diesel particles, P1, P2, and P3. P1 is emitted at 06:05 LST and always contains water. P2 is emitted at 06:56 LST and is initially dry but becomes wet in the afternoon. P3 is emitted at 16:18 LST later in the day when little condensation occurs.

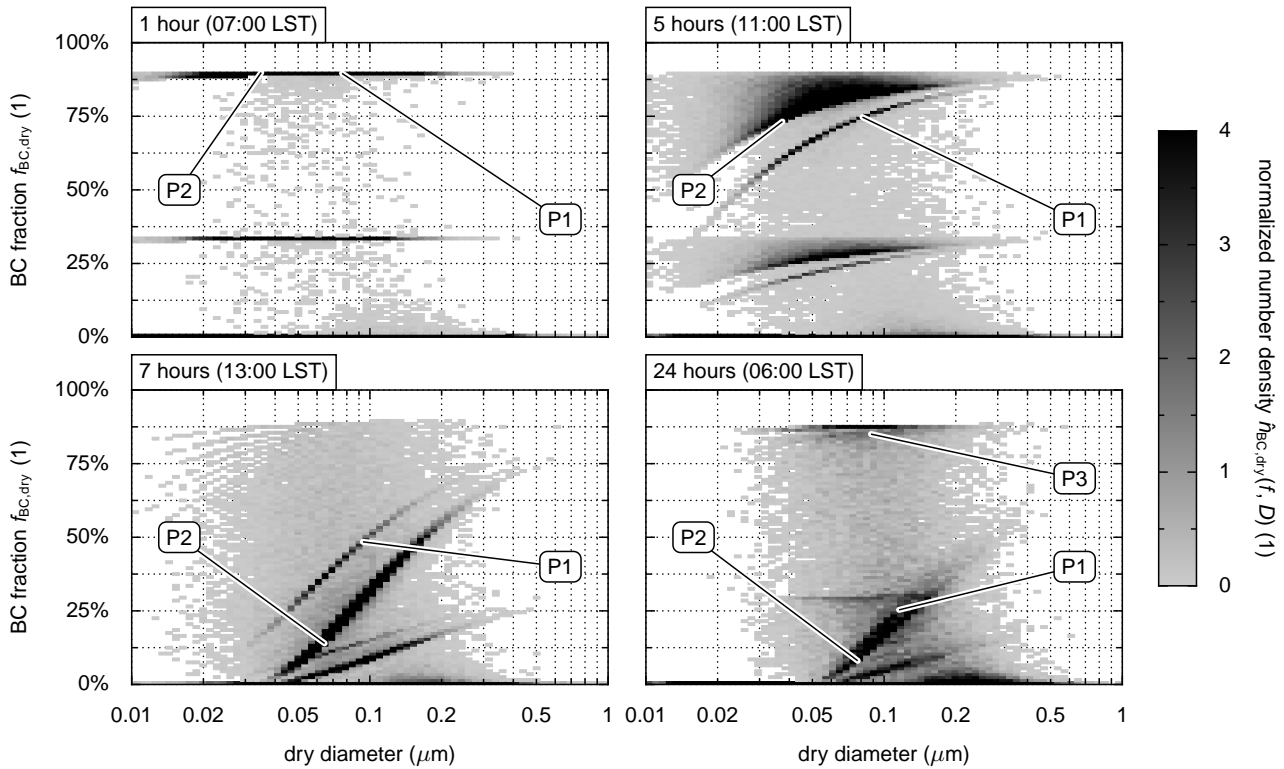


Figure 10. Normalized two-dimensional number distribution $\hat{n}_{BC,dry}(f, D)$ after 1, 5, 7, and 24 hours of simulation. The labels P1, P2, and P3 track three individual diesel emission particles as they evolve over the course of the simulation. The maximum plotted value for $\hat{n}_{BC,dry}(f, D)$ is capped at 4 to allow better resolution.

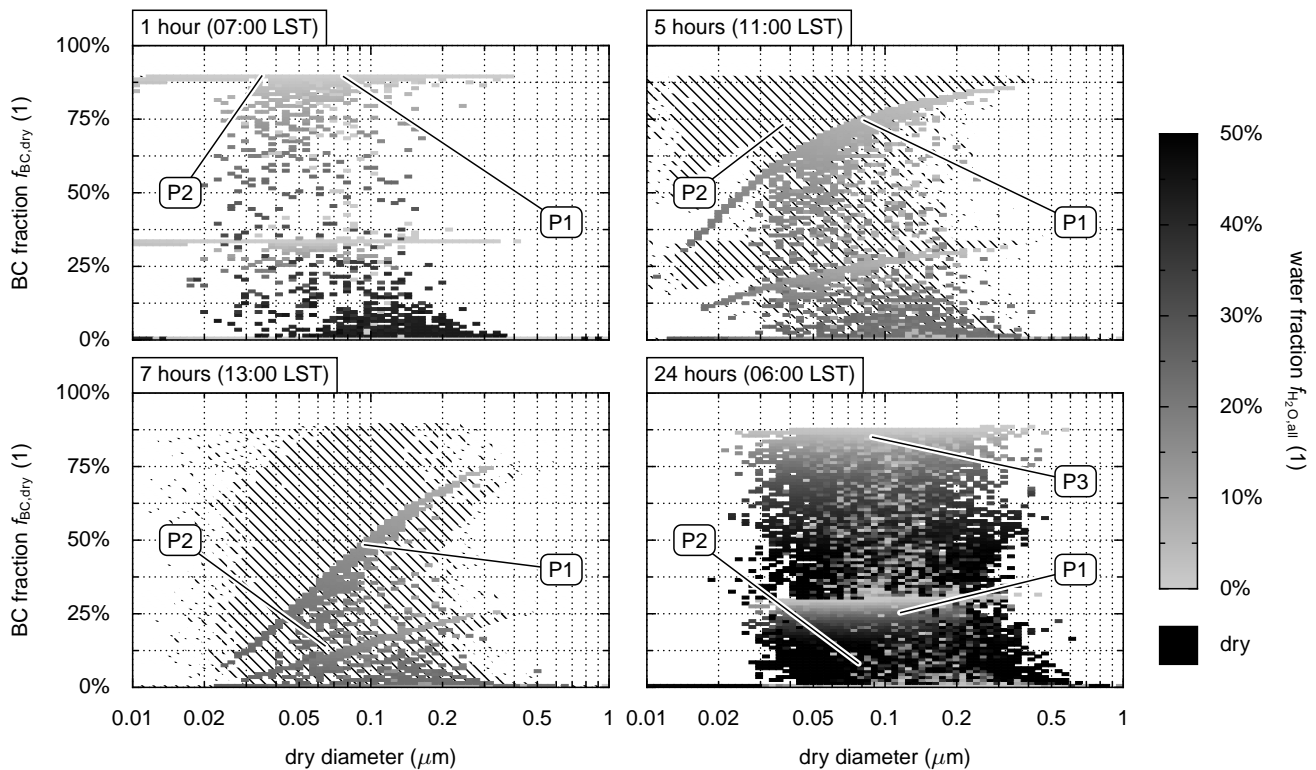


Figure 11. Water fraction, $f_{H_2O,all}$ as a function of BC fraction $f_{BC,dry}$ and dry diameter after 1, 5, 7, and 24 hours of simulation. The labels P1, P2, and P3 track three individual diesel emission particles as they evolve over the course of the simulation. Note that the water fraction of wet particles is plotted over the hashing for dry particles and sometimes obscures it. In particular, after 1 hour (07:00 LST) there are dry diesel and gasoline particles present but they are not visible. The water fraction plotted for a given two-dimensional bin is the minimum of the water fraction for all wet particles in that bin. For example, after 24 hours the particle P1 is very wet (see Figure 9) but there are much drier particles present with similar composition, giving a low $f_{H_2O,all}$ value on the plot at P1. The maximum plotted value for $f_{H_2O,all}$ is capped at 50% to allow better resolution.

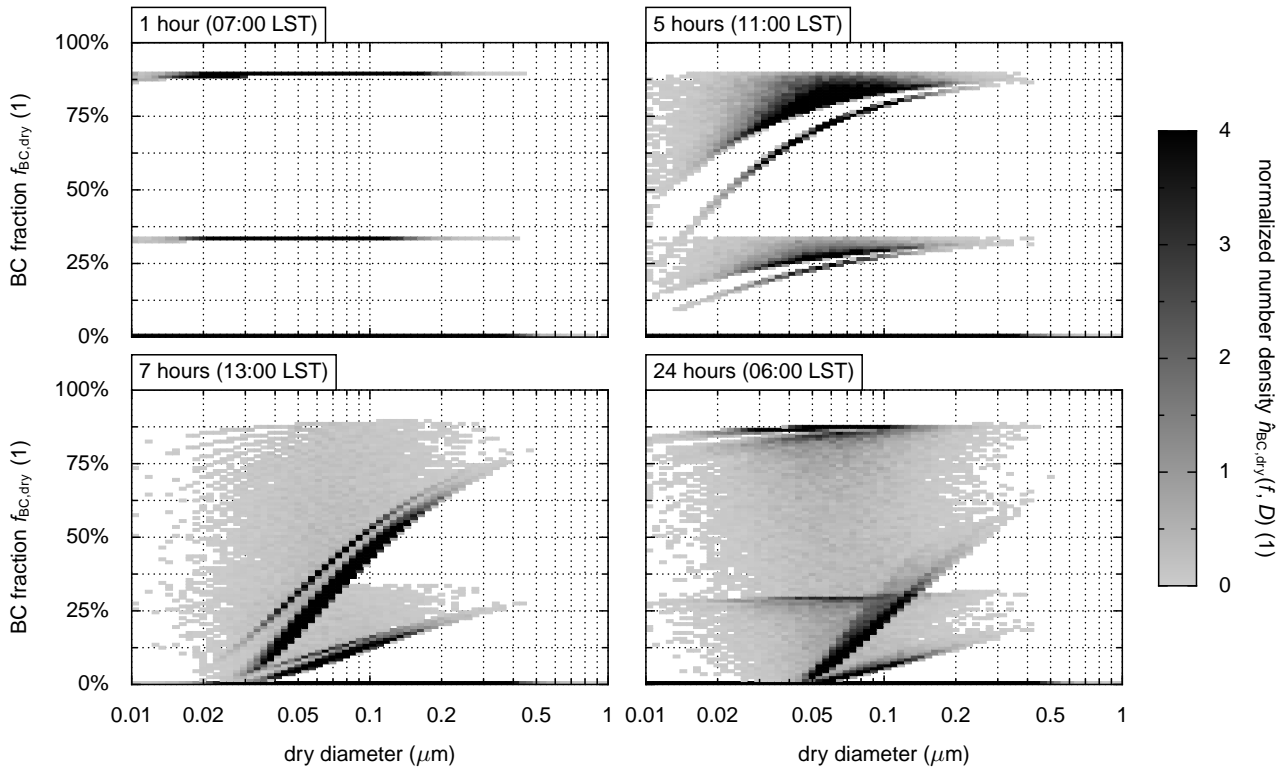


Figure 12. Normalized two-dimensional number distribution $\hat{n}_{BC,dry}(f, D)$ after 1, 5, 7, and 24 hours of simulation, as in Figure 10, but for the simulation without coagulation. The maximum plotted value for $\hat{n}_{BC,dry}(f, D)$ is capped at 4 to allow better resolution.

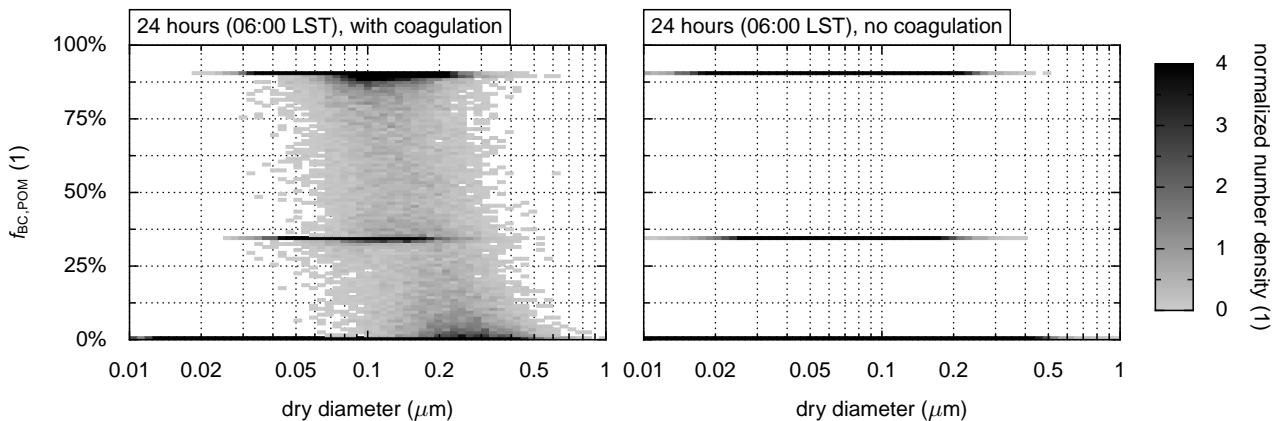


Figure 13. Normalized two-dimensional number distribution $\hat{n}_{BC,POM}(f, D)$ after 24 hours of simulation (06:00 LST the following day), with and without coagulation. The maximum plotted value for $\hat{n}_{BC,dry}(f, D)$ is capped at 4 to allow better resolution.

ity reached 61% in the following afternoon at 16:00 LST. Hence, between 06:46 and 16:00 LST, wet and dry particles co-existed in the air parcel. Particle P1 in Figures 10 and 11 is one of the particles that was emitted early and stayed wet throughout the simulation, whereas particle P2 started out dry and became wet only in the afternoon. For the wet and dry particles different thermodynamic equilibria applied which was reflected in the different development of their $f_{BC,dry}$ values.

As the single-particle plot Figure 9 shows, the wet particles contained nitrate from the beginning and kept taking up nitrate, while during the first few hours vapor pressures of HNO_3 and NH_3 were too low to allow nitrate formation on dry particles. Due to this difference in nitrate formation,

after 5 hours (11:00 LST) the wet particles appear distinct from the dry particles in Figure 10 and reached lower $f_{BC,dry}$ values, reflecting their larger ammonium nitrate content.

This changed after 11:30 LST. At this time HNO_3 and NH_3 were high enough so that ammonium nitrate formed on the dry particles. They accumulated ammonium nitrate quickly, and $f_{BC,dry}$ decreased rapidly for the dry particles. As a result, $f_{BC,dry}$ of the dry particles fell below $f_{BC,dry}$ of the wet particles, as is evident in the graph for 7 hours (13:00 LST) in Figures 10 and 11.

After 18:00 LST the ammonium nitrate formations stopped, as NH_3 concentration dropped to near zero (compare Figure 6). Therefore the fresh particle emissions after this time did not accumulate much condensable material and stayed at high $f_{BC,dry}$ values. This is reflected in the single-

particle plot Figure 9, which shows the diesel particle P3 that was emitted in the afternoon. The mass of secondary species for this particle was much lower than its BC content. After 12 hours (18:00 LST) both particle and gas emissions stopped, and the particle distribution changed mainly due to coagulation and dilution. The particle number decreased as a result of coagulation and continued dilution with the background, but this effect is not visible in the normalized number densities. During the evening hours the relative humidity increased again and particles took up a substantial amount of water. As the 24 hour plot in Figure 11 shows, the water content depended on the mixing state, i.e. for a given size we find particles with water mass-fractions between near 0% and 66%.

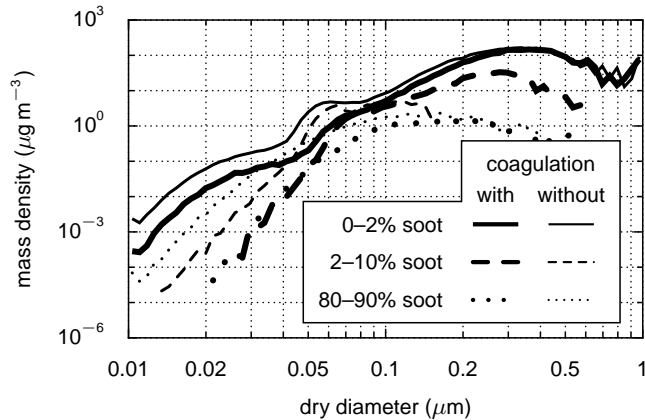


Figure 14. Mass distribution after 24 hours (06:00 LST the following day) for three different mixing state ranges: $m_{\text{BC,dry}}([0\%, 2\%], D)$, $m_{\text{BC,dry}}([2\%, 10\%], D)$, and $m_{\text{BC,dry}}([80\%, 90\%], D)$, as defined in equation (30). The cases with and without coagulation are plotted for comparison.

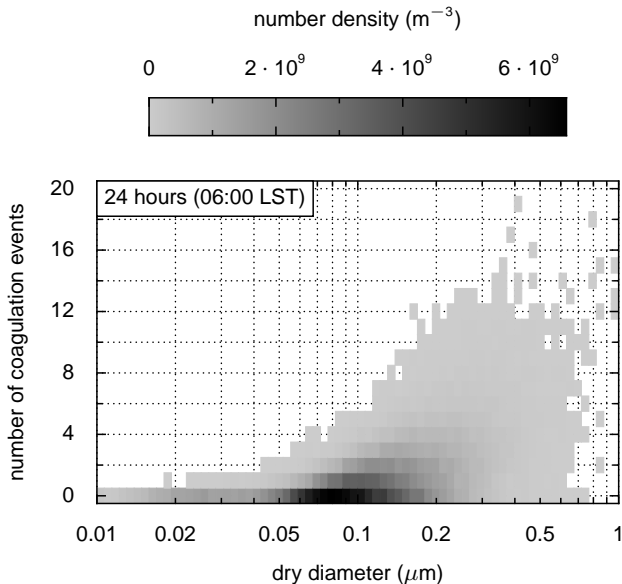


Figure 15. Two-dimensional number distribution $n_{\text{coag}}(k, D)$ showing the number of coagulation events experienced after 24 hours (06:00 LST the following day), as defined in equation (7). The maximum plotted value for $n_{\text{coag}}(k, D)$ is capped at $6 \cdot 10^9 \text{ m}^{-3}$ to allow better resolution.

Comparing the result for the end of the simulation to the results at previous times, we note that at the end of the simulation particles below $D = 0.03 \mu\text{m}$ were depleted due to coagulation. A continuum of mixing states formed in between the extreme mixing states of $f_{\text{BC,dry}} = 0\%$ and $f_{\text{BC,dry}} = 90\%$.

The comparison to the case without coagulation gives results as displayed in Figure 12. This figure is analogous to Figure 10 and shows the mixing state $f_{\text{BC,dry}}$ of BC with respect to the sum of all other substances. Without coagulation similar frontal features appeared, but diesel particles and gasoline particles remained more clearly distinct until 6 hours of simulation (12:00 LST) without the mixing effect of coagulation. After about 12:00 LST the mixing state became continuous, because the most aged diesel car emissions started overlapping with the relatively fresh gasoline emission particles. However, since these mixing states were formed due to condensation only, an internal mixture of primary species such as POM and BC existed only when the particles were emitted as this mixture. After 24 hours of simulation without coagulation, mixed particles smaller than $D = 0.03 \mu\text{m}$ were still present while they were depleted in Figure 10 with coagulation.

The impact of coagulation on the mixing state with respect to the primary components BC and POM is shown in Figure 13. The left figure displays the BC mixing state with respect to POM, $f_{\text{BC,POM}}$, after 24 hours with coagulation. POM was emitted as a constituent of primary particles, which can be seen as horizontal lines with high number densities at $f_{\text{BC,POM}} = 90\%$ for diesel car emissions, $f_{\text{BC,POM}} = 34\%$ for gasoline car emissions and $f_{\text{BC,POM}} = 0\%$ for meat cooking emissions. The mixing states between these could only form as a result of coagulation. Since coagulation is most efficient between particles of different size, we observe that these mixed particles preferentially formed in a specific size range. For sizes larger than $D = 0.05 \mu\text{m}$, POM/BC mixtures of various degree of mixing formed due to coagulation. Below $0.05 \mu\text{m}$, coagulation produced very few particles, so particles at these sizes were at their initial BC/POM mixing state. Nearly all particles below $0.03 \mu\text{m}$ were removed by coagulation. For comparison the right panel of Figure 13 shows the BC mixing state with respect to POM, $f_{\text{BC,POM}}$, at the end of the simulation without coagulation. For this case the intermediate mixing states did not occur, and particles below $D = 0.03 \mu\text{m}$ remained.

Figure 14 shows the one-dimensional size distributions of total mass density (including water) for different ranges of mixing states at the end of the simulation, comparing the cases with and without coagulation. From this we see that coagulation did not simply reduce the number densities, but also shifted black carbon mass within the diameter- $f_{\text{BC,dry}}$ space. The mass of particles smaller than $D = 0.05 \mu\text{m}$ with high BC content ($f_{\text{BC,dry}}$ between 80% and 90%) was reduced by 90% due to coagulation. The mass of particles smaller than $D = 0.05 \mu\text{m}$ with very low BC content ($f_{\text{BC,dry}}$ between 0% and 2% BC) was reduced by 81% when coagulation was included. A very large difference between the cases with and without coagulation occurred for $f_{\text{BC,dry}}$ between 2% and 10% and for the size range above $D = 0.1 \mu\text{m}$. Mass in this range of parameters arose mainly from coagulation of large, BC-free particles with small BC-containing particles and this mass increased by 1458% when coagulation was included.

With PartMC it is straightforward to track the number of coagulation events experienced by the individual particles. Figure 15 shows the two-dimensional number distribution $n(k, D)$, with k being the number of coagulation events. At the end of the simulation, 5% of particles had undergone at least 5 coagulation events. The largest number of coagulation events was 19 and occurred for particles on the right hand side of the spectrum with sizes larger than $D = 0.4 \mu\text{m}$. Given a certain size, the number of coagulation events varied, which shows the stochastic nature of the coagulation process. The range of variation was greater for larger particles. For example, while the number of coagulation events varied between 0 and 5 for a $D = 0.1 \mu\text{m}$ particle, it ranged between 0 and 12 for a $D = 0.3 \mu\text{m}$ particle.

6. Summary

In this paper we presented the development and the application of a stochastic particle-resolved aerosol model, PartMC-MOSAIC. It explicitly resolves the composition of individual particles in a given population of different types of aerosol particles, and accurately tracks their evolution due to emission, dilution, condensation and coagulation. To make the direct stochastic particle-based method practical, we implemented an accelerated coagulation method. With this method we achieved optimal efficiency for applications when the coagulation kernel is highly non-uniform, as is the case for many realistic environments. The highly accurate treatment of aerosol dynamics and chemistry makes PartMC-MOSAIC suitable for use as a numerical benchmark of mixing state for more approximate models. The current version of PartMC is available under the GNU General Public License (GPL) at <http://www.meche.uiuc.edu/research/mwest/partmc/>, and the MOSAIC code is available upon request from R. A. Zaveri.

PartMC-MOSAIC was applied to an idealized example urban plume case to simulate the evolution of urban aerosols of different types due to coagulation and condensation, focusing on the aging process of BC. For the first time results of the aerosol composition and size distribution are available as a fully multi-dimensional size distribution without any a priori assumptions about the mixing state. This detail of information was only achievable with a particle-resolved model.

To display the results, we projected the multi-dimensional size distributions to two-dimensional distributions depending on particle size and BC mass ratio. We specifically discussed the results for BC mass ratios defined with respect to all other dry constituents, $f_{BC,dry}$, and to POM, $f_{BC,POM}$. Due to the diurnal variations in temperature, relative humidity, and gas phase concentrations, the thermodynamic equilibrium conditions for the ammonium-sulfate-nitrate system changed continuously. The aerosol hydration hysteresis effect led to the co-existence of metastable (wet) and stable (dry) particles in the air parcel during the daytime, depending on their time of emission. Since the formation of ammonium nitrate depends on the particle phase state, this in turn resulted in pronounced differences in how the aging proceeded. As a result of coagulation and condensation, after 24 hours of simulation, the aerosol population evolved into a state where a continuum of BC mixing states existed. Coagulation was effective in removing smaller particles, reducing number densities by 84%, 66%, and 29% at diameters of 0.05, 0.07, and 0.10 μm in the example simulation.

Acknowledgments. Funding for N. Riemer and M. West was provided by the National Science Foundation (NSF) under grant ATM 0739404.

Funding for R. A. Zaveri and R. C. Easter was provided by the Aerosol-Climate Initiative as part of the Pacific Northwest National Laboratory (PNNL) Laboratory Directed Research and Development (LDRD) program. Pacific Northwest National Laboratory is operated for the U.S. Department of Energy by Battelle Memorial Institute under contract DE-AC06-76RLO 1830.

References

- Adams, P. J., J. H. Seinfeld, and D. M. Koch (1999), Global concentration of tropospheric sulphate, nitrate and ammonium simulated in a general circulation model, *J. Geophys. Res.*, *104*, 13,791–13,823.
- Alfonso, L., G. Raga, and D. Baumgardner (2008), Monte Carlo simulations of two-component drop growth by stochastic coalescence, *Atmos. Chem. Phys. Discuss.*, *8*, 7289–7313.
- Anderson, D. (2007), A modified next reaction method for simulating chemical systems with time dependent propensities and delays, *J. Chem. Phys.*, *127*, 214,107, doi:10.1063/1.2799998.
- Anderson, D. (2008), Incorporating postleap checks in tau-leaping, *J. Chem. Phys.*, *128*, 054,103, doi:10.1063/1.2819665.
- Andreae, M., and A. Gelencsér (2006), Black carbon or brown carbon? The nature of light-absorbing carbonaceous aerosols, *Atmos. Chem. Phys.*, *6*, 3131–3148.
- Andreae, M. O., R. J. Charlson, F. Bruynseels, H. Storms, and R. V. Grieken (1986), Internal mixture of sea salt, silicates, and excess sulfate in marine aerosols, *Science*, *232*, 1620–1623.
- Babovsky, H. (1999), On a Monte Carlo scheme for Smoluchowski's coagulation equation, *Monte Carlo Methods and Applications*, *5*(1), 1–18.
- Bhave, P. V., M. J. Kleeman, J. O. Allen, and L. S. Hughes (2002), Evaluation of an air quality model for the size and composition of source-oriented particle classes, *Environ. Sci. Technol.*, *36*, 2154–2163.
- Binkowski, F. S., and U. Shankar (1995), The regional particulate matter model, 1. model description and preliminary results, *J. Geophys. Res.*, *100*, 26,191–26,209.
- Bond, T. C., G. Habib, and R. W. Bergstrom (2006), Limitations in the enhancement of visible light absorption due to mixing state, *J. Geophys. Res.*, *111*, D20,211, doi:10.1029/2006JD007215.
- Bott, A. (1998), A flux method for the numerical solution of the stochastic collection equation, *J. Atmos. Sci.*, *55*, 2284–2293.
- Brock, J. R., P. J. Kuhn, and D. Zehavi (1988), Formation and growth of binary aerosol in a laminar coaxial jet, *J. Aerosol Sci.*, *19*, 413–424.
- California Air Resources Board (2007), Emissions database: 2006 Estimated annual average emissions, <http://www.arb.ca.gov/ei/emissiondata.htm>, accessed in October, 2007.
- Cao, Y., D. T. Gillespie, and L. R. Petzold (2005), The slow-scale stochastic simulation algorithm, *The Journal of Chemical Physics*, *122*, 014,116.
- Cao, Y., D. T. Gillespie, and L. R. Petzold (2006), Efficient step-size selection for the tau-leaping simulation method, *J. Chem. Phys.*, *124*, 044,109, doi:10.1063/1.2159468.
- Chung, S. H., and J. H. Seinfeld (2002), Global distribution and climate forcing of carbonaceous aerosols, *J. Geophys. Res.*, *107*, doi:10.1029/2001JD001397.
- Chung, S. H., and J. H. Seinfeld (2005), Climate response of direct radiative forcing of anthropogenic black carbon, *J. Geophys. Res.*, *111*, D11,102.
- Chýlek, P., G. Videen, D. Ngo, R. G. Pinnek, and J. D. Klett (1995), Effect of black carbon on the optical properties and climate forcing of sulfate aerosols, *J. Geophys. Res.*, *100*, 16,325–16,332.
- Clarke, A. D., and K. J. Noone (1985), Soot in the Arctic snowpack: A cause for perturbations in radiative transfer, *Atmos. Environ.*, *19*, 2045–2053.
- Cooke, W. F., C. Lioussé, H. Cachier, and J. Feichter (1999), Construction of a $1^\circ \times 1^\circ$ fossil fuel emission data set for carbonaceous aerosol and implementation and radiative impact in the ECHAM4 model, *J. Geophys. Res.*, *104*, 22,137–22,162.
- Croft, B., U. Lohmann, and K. von Salzen (2005), Black carbon aging in the Canadian Centre for Climate modelling and analysis atmospheric general circulation model, *Atmos. Chem. Phys.*, *5*, 1931–1949, sRef-ID:1680-7324/acp/2005-5-1931.
- Cubison, M. J., B. Ervens, G. Feingold, K. S. Docherty, I. M. Ulbrich, L. Shields, K. Prather, S. Hering, and J. L. Jimenez (2008), The influence of chemical composition and mixing state on Los Angeles urban aerosol on CCN number and cloud properties., *Atmos. Chem. Phys. Discuss.*, *8*, 5629–5681.
- Debry, E., B. Sportisse, and B. Jourdain (2003), A stochastic approach for the numerical simulation of the general dynamics equations for aerosols, *Journal of Computational Physics*, *184*(2), 649–669, doi:10.1016/S0021-9991(02)00041-4.
- Dhaniyala, S., and A. S. Wexler (1996), Numerical schemes to model condensation and evaporation of aerosols, *Atmos. Environ.*, *30*, 919–928.
- Ducret, J., and H. Cachier (1992), Particulate carbon in rain at various temperate and tropical locations, *J. Atmos. Chem.*, *15*, 55–67.
- E, W., D. Liu, and E. Vanden-Eijnden (2007), Nested stochastic simulation algorithm for chemical kinetic systems with multiple time scales, *J. Computational Phys.*, *221*, 158–180.

- Efendiev, Y., and M. R. Zachariah (2002), Hybrid Monte Carlo method for simulation of two-component aerosol coagulation and phase segregation, *Journal of Colloid and Interface Science*, *249*, 30–43, doi:10.1006/jcis.2001.8114.
- Eibeck, A., and W. Wagner (2001), Stochastic particle approximation for Smoluchowski's coagulation equation, *The Annals of Applied Probability*, *11*(4), 1137–1165, doi:10.1214/aoap/1015345398.
- El Samad, H., M. Khammash, L. Petzold, and D. Gillespie (2005), Stochastic modeling of gene regulatory networks, *International Journal of Robust and Nonlinear Control*, *15*(15), 691–711.
- Eldering, A., and G. R. Cass (1996), Source-oriented model for air pollution effects on visibility, *J. Geophys. Res.*, *101*, 19,343–19,369.
- Fassi-Fihri, A., K. Suhre, and R. Rosset (1997), Internal and external mixing in atmospheric aerosols by coagulation: Impact on the optical and hygroscopic properties of the sulphate-soot system, *Atmos. Environ.*, *31*, 1393–1402.
- Fichthorn, K. A., and W. H. Weinberg (1991), Theoretical foundations of dynamical Monte Carlo simulations, *J. Chem. Phys.*, *95*(2), 1090–1096.
- Garcia, A. L., C. van den Broek, M. Aertsens, and R. Serneels (1987), A Monte Carlo method of coagulation, *Physica*, *143A*, 535–546.
- Gibson, M., and J. Bruck (2000), Efficient exact stochastic simulation of chemical systems with many species and many channels, *J. Phys. Chem. A*, *104*, 1876–1889.
- Gillespie, D. T. (1972), The stochastic coalescence model for cloud droplet growth, *J. Atmos. Sci.*, *29*, 1496–1510.
- Gillespie, D. T. (1975), An exact method for numerically simulating the stochastic coalescence process in a cloud, *J. Atmos. Sci.*, *32*, 1977–1989.
- Gillespie, D. T. (1976), A general method for numerically simulating the stochastic time evolution of coupled chemical reactions, *J. Comput. Phys.*, *22*, 403–434.
- Gillespie, D. T. (1977), Exact stochastic simulation of coupled chemical reactions, *J. Phys. Chem.*, *81*, 2340–2361, doi:10.1021/j100540a008.
- Gillespie, D. T. (1992), *Markov Processes: An Introduction for Physical Scientists*, Academic Press.
- Gillespie, D. T. (2001), Approximate accelerated stochastic simulation of chemically reacting systems, *J. Chem. Phys.*, *115*(4), 1716–1733.
- Gillespie, D. T. (2007), Stochastic simulation of chemical kinetics, *Annual Review of Physical Chemistry*, *58*, 35–55, doi:10.1146/annurev.physchem.58.032806.104637.
- Gillespie, D. T., and L. R. Petzold (2003), Improved leap-size selection for accelerated stochastic simulation, *J. Chem. Phys.*, *119*, 8229, doi:10.1063/1.1613254.
- Guías, F. (1997), A Monte Carlo approach to the Smoluchowski equations, *Monte Carlo Methods Appl.*, *3*, 313–326.
- Hansen, J., and L. Nazarenko (2004), Soot climate forcing via snow and ice albedos, *PNAS*, *101*, 423–428.
- Horvath, H., and A. Trier (1993), A study of the aerosol of Santiago de Chile — I. Light extinction coefficient, *Atmos. Environ.*, *27*, 371–384.
- Jacobson, M. Z. (1997), Development and application of a new air pollution modeling system — II. Aerosol module structure and design, *Atmos. Environ.*, *31*, 131–144.
- Jacobson, M. Z. (1999), *Fundamentals of Atmospheric Modeling*, Cambridge University Press, Cambridge.
- Jacobson, M. Z. (2000), A physically based treatment of elemental carbon optics: Implications for global direct forcing of aerosols, *Geophys. Res. Lett.*, *27*, 217–220.
- Jacobson, M. Z. (2001), Strong radiative heating due to the mixing state of black carbon in atmospheric aerosols, *Nature*, *409*, 695–697.
- Jacobson, M. Z. (2002a), Analysis of aerosol interactions with numerical techniques for solving coagulation, nucleation, condensation, dissolution, and reversible chemistry among multiple size distributions, *J. Geophys. Res.*, *107*, 4366.
- Jacobson, M. Z. (2002b), Control of fossil-fuel particulate black carbon and organic matter, possibly the most effective method of slowing global warming, *J. Geophys. Res.*, *107*, 4410, doi:10.1029/2011JD001376.
- Jaenicke, R. (1993), *Aerosol-Cloud-Climate Interaction*, chap. Tropospheric aerosols, pp. 1–31, Academic Press, San Diego, CA.
- Johnson, K. S., B. Zuberi, L. T. Molina, M. J. Molina, M. J. Iedema, J. P. Cowin, D. J. Gaspar, C. Wang, and A. Laskin (2005), Processing of soot in an urban environment: case study from the Mexico City Metropolitan Area, *Atmos. Chem. Phys.*, *5*, 3033–3043, sRef-ID: 1680-7324/acp/2005-5-3033.
- Kittelson, D., W. Watts, and J. Johnson (2006a), On-road and laboratory evaluation of combustion aerosols — Part 1: Summary of diesel engine results, *Aerosol Sci.*, *37*, 913–930.
- Kittelson, D., W. Watts, J. Johnson, J. Schauer, and D. Lawson (2006b), On-road and laboratory evaluation of combustion aerosols — Part 2: Summary of spark ignition engine results, *Aerosol Sci.*, *37*, 931–949.
- Kleeman, M. J., and G. R. Cass (1998), Source contributions to the size and composition distribution of urban particulate air pollution, *Atmos. Environ.*, *32*, 2803–2816.
- Kleeman, M. J., G. R. Cass, and A. Eldering (1997), Modeling the airborne particle complex as a source-oriented external mixture, *J. Geophys. Res.*, *102*, 21,355–21,372.
- Kleeman, M. J., L. S. Hughes, J. Allen, and G. R. Cass (1999), Source contributions to the size and composition distribution of atmospheric particles: Southern California in September 1996, *Environ. Sci. Technol.*, *33*, 4331–4341.
- Kleeman, M. J., A. Eldering, J. R. Hall, and G. R. Cass (2001), Effect of emissions control programs on visibility in Southern California, *Environ. Sci. Technol.*, *35*, 4668–4674.
- Koch, D. (2001), Transport and direct radiative forcing of carbonaceous and sulfate aerosols in the GISS GCM, *J. Geophys. Res.*, *106*, 20,311–20,332.
- Kolodko, A., and K. Sabelfeld (2003), Stochastic particle methods for Smoluchowski coagulation equation: variance reduction and error estimations, *Monte Carlo Methods and Applications*, *9*(4), 315–339, doi:10.1163/156939603322601950.
- Kruis, F. E., A. Maisels, and H. Fissan (2000), Direct simulation Monte Carlo method for particle coagulation and aggregation, *AIChE*, *46*, 1735–1742.
- Laurenzi, I. J., J. D. Bartels, and S. L. Diamond (2002), A general algorithm for exact simulation of multicomponent aggregation processes, *Journal of Computational Physics*, *177*, 418–449, doi:10.1006/jcph.2002.7017.
- Lesins, G., P. Chylek, and U. Lohmann (2002), A study of internal and external mixing scenarios and its effect on aerosol optical properties and direct radiative forcing, *J. Geophys. Res.*, *107*, 4094, doi:10.1029/2001JD000973.
- Levin, Z. L., E. Ganor, and V. Gladstein (1996), The effects of desert particles coated with sulfate on rain formation in the eastern Mediterranean, *J. Appl. Meteorol.*, *35*, 1511–1523.
- Lohmann, U., J. Feichter, C. C. Chuang, and J. E. Penner (1999), Prediction of the number of cloud droplets in the ECHAM GCM, *J. Geophys. Res.*, *104*, 9169–9198.
- Maisels, A., F. E. Kruis, and H. Fissan (2004), Direct simulation Monte Carlo for simultaneous nucleation, coagulation, and surface growth in dispersed systems, *Chemical Engineering Science*, *59*, 2231–2239.
- McGraw, R. (1997), Description of aerosol dynamics by the quadrature method of moments, *Aerosol Sci. Technol.*, *27*, 255–265.
- Medalia, A., and D. Rivin (1982), Particulate carbon and other components of soot and carbon black, *Carbon*, *20*, 481–492.
- Menon, S., J. Hansen, L. Nazarenko, and Y. F. Luo (2002), Climate effects of black carbon aerosols in China and India, *Science*, *297*, 2250–2253.
- Nenes, A., W. C. Conant, and J. H. Seinfeld (2002), Black carbon radiative heating effects on cloud microphysics and implications for the aerosol indirect effect - 2. Cloud microphysics, *J. Geophys. Res.*, *107*, 4605, doi:10.1029/2002JD002101.
- Okada, K., and R. M. Hitznerberger (2001), Mixing properties of individual submicrometer aerosol particles in Vienna, *Atmos. Environ.*, *35*, 5617–5628.
- Penner, J. E. (1995), *Aerosol Forcing and Climate*, chap. Carbonaceous aerosols influencing atmospheric radiation: Black and organic carbon, pp. 91–108, John Wiley, New York.
- Pope, A., and D. Dockery (1996), Epidemiology of chronic health effects: Cross-sectional studies, in *Particles in Our Air: Concentrations and Health Effects*, edited by R. W. and J. Sprengrer, pp. 149–168, Harvard University Press, Cambridge, MA.
- Rathinam, M., L. R. Petzold, Y. Cao, and D. T. Gillespie (2003), Stiffness in stochastic chemically reacting systems: The implicit tau-leaping method, *J. Chem. Phys.*, *119*, 12,784, doi:10.1063/1.1627396.

- Riemer, N., H. Vogel, B. Vogel, and F. Fiedler (2003), Modeling aerosols on the mesoscale γ , part I: Treatment of soot aerosol and its radiative effects, *J. Geophys. Res.*, *108*, 4601, doi:10.1029/2003JD003448.
- Roeckner, E., P. Stier, J. Feichter, S. Kloster, M. Esch, and I. Fischer-Bruns (2006), Impact of carbonaceous aerosol emissions on regional climate change, *Clim. Dyn.*, *27*, 553–571.
- Saathoff, H., K.-H. Naumann, N. Riemer, S. Kamm, O. Möhler, U. Schurath, H. Vogel, and B. Vogel (2001), The loss of NO₂, HNO₃, NO₃/N₂O₅, and HO₂/HOONO₂ on soot aerosol: A chamber and modeling study, *Geophys. Res. Lett.*, *28*, 1957–1960.
- Schell, B., I. J. Ackermann, F. S. Binkowski, and A. Ebel (2001), Modeling the formation of secondary organic aerosol within a comprehensive air quality model system, *J. Geophys. Res.*, *106*, 28,275–28,293.
- Schnaiter, M., C. Linke, O. Möhler, K.-H. Naumann, H. Saathoff, R. Wagner, and B. Wehner (2005), Absorption amplification of black carbon internally mixed with secondary organic aerosol, *J. Geophys. Res.*, *110*, D19,204, doi:10.1029/2005JD006046.
- Spouge, J. L. (1985), Monte Carlo results for random coagulation, *Journal of Colloid and Interface Science*, *107*(1), 38–43.
- Stier, P., et al. (2005), The aerosol-climate model ECHAM5-HAM, *Atmos. Chem. Phys.*, *5*, 1125–1156.
- Tsigaridis, K., and M. Kanakidou (2003), Global modeling of secondary organic aerosol in the troposphere: A sensitivity analysis, *Atmos. Chem. Phys.*, *3*, 1849–1869, sRef-ID: 1680-7324/acp/2003-3-1849.
- von Smoluchowski, M. (1916a), Drei Vorträge über Diffusion, Brownsche Molekularbewegung und Koagulation von Kolloidteilchen, *Phys. Z.*, *17*, 557–571, 585–599.
- von Smoluchowski, M. (1916b), Versuch einer mathematischen Theorie der Koagulationskinetik kolloider Lösungen, *Z. Phys. Chem.*, *92*, 129–168.
- Weingartner, E., H. Burtscher, and H. Baltensperger (1997), Hygroscopic properties of carbon and diesel soot particles, *Atmos. Environ.*, *31*, 2311–2327.
- Wells, C., N. Morgan, M. Kraft, and W. Wagner (2006), A new method for calculating the diameters of partially-sintered nanoparticles and its effect on simulated particle properties, *Chem. Eng. Sci.*, *61*, 158–166.
- Wexler, A. S., F. W. Lurmann, and J. H. Seinfeld (1994), Modelling urban aerosols - I. model development, *Atmos. Environ.*, *28*, 531–546.
- Whitby, E. R., and P. H. McMurray (1997), Modal aerosol dynamics modeling, *Aerosol Sci. Technol.*, *27*, 673–688.
- Whitby, E. R., P. H. McMurray, U. Shankar, and F. S. Binkowski (1991), Modal Aerosol Dynamics Modeling, *Tech. Rep. 600/3-91/020*, (NTIS PB91-161729/AS Natl. Tech. Inf. Serv. Springfield, Va.), Atmos. Res. and Exposure Assess. Lab. U.S. Environ. Prot. Agency, Research Triangle Park, N.C.
- Wilson, J., C. Cuvelier, and F. Raes (2001), A modeling study of global mixed aerosol fields, *J. Geophys. Res.*, *106*, 34,081–34,108.
- Wu, C.-Y., and P. Biswas (1998), Study of numerical diffusion in a discrete-sectional model and its application to aerosol dynamics simulation, *Aerosol Sci. and Technol.*, *29*, 359–378.
- Ying, Q., and M. J. Kleeman (2006), Source contributions to the regional distribution of secondary particulate matter in California, *Atmos. Environ.*, *40*, 736–752.
- Ying, Q., M. Mysliviec, and M. J. Kleeman (2004), Source apportionment of visibility impairment using a three-dimensional source-oriented air quality model, *Environ. Sci. Technol.*, *38*, 1089–1101.
- Yoon, C., and R. McGraw (2004a), Representation of generally mixed multivariate aerosols by the quadrature method of moments: I. Statistical foundation, *Aerosol Science*, *35*, 561–576, doi:10.1016/j.jaerosci.2003.11.003.
- Yoon, C., and R. McGraw (2004b), Representation of generally mixed multivariate aerosols by the quadrature method of moments: II. Aerosol dynamics, *Aerosol Science*, *35*, 577–598, doi:10.1016/j.jaerosci.2003.11.012.
- Zaveri, R. A., and L. K. Peters (1999), A new lumped structure photochemical mechanism for large-scale applications, *J. Geophys. Res.*, *104*, 30,387–30,415.
- Zaveri, R. A., R. C. Easter, and L. K. Peters (2005a), A computationally efficient Multicomponent Equilibrium Solver for Aerosols (MESA), *J. Geophys. Res.*, *110*, D24,203, doi:10.1029/2004JD005618.
- Zaveri, R. A., R. C. Easter, and A. S. Wexler (2005b), A new method for multicomponent activity coefficients of electrolytes in aqueous atmospheric aerosols, *J. Geophys. Res.*, *110*, D02,210, doi:10.1029/2004JD004681.
- Zaveri, R. A., R. C. Easter, J. D. Fast, and L. K. Peters (2008), A new model for simulating aerosol interactions and chemistry (MOSAIC), *J. Geophys. Res.*, doi:10.1029/2007JD008782, (in press).
- Zhang, K. M., and A. S. Wexler (2002), Modeling the number distributions of urban and regional aerosols: theoretical foundations, *Atmos. Environ.*, *36*, 1863–1874.

N. Riemer, Department of Atmospheric Science, University of Illinois at Urbana-Champaign, 105 S. Gregory St., Urbana, IL 61801, USA. (nriemer@illinois.edu)

M. West, Department of Mechanical Science and Engineering, University of Illinois at Urbana-Champaign, 1206 W. Green St., Urbana, IL 61801, USA. (mwest@illinois.edu)

R. A. Zaveri, Atmospheric Science and Global Change Division, Pacific Northwest National Laboratory, MSIN K9-30, P.O. Box 999, Richland, WA 99352, USA. (rahul.zaveri@pnl.gov)

R. C. Easter, Atmospheric Science and Global Change Division, Pacific Northwest National Laboratory, MSIN K9-30, P.O. Box 999, Richland, WA 99352, USA. (richard.easter@pnl.gov)